# The RESOLVE project: a multi-physics experiment with a temporary dense seismic array on the Argentière Glacier, French Alps

Florent Gimbert, Ugo Nanni, Philippe Roux, A. Helmstetter, S. Garambois, A. Lecointre, A. Walpersdorf, B. Jourdain, M. Langlais, O. Laarman, et al.

# The RESOLVE project: a multi-physics experiment with a temporary dense seismic array on the Argentière Glacier, French Alps

Gimbert, F.[1], U. Nanni[1], P. Roux[2], A. Helmstetter[2], S. Garambois[2], A. Lecointre[2], A. Walpersdorf[2], B. Jourdain[1], M. Langlais[2], O. Laarman[1], F. Lindner[3], A. Sergeant[4], C. Vincent[1], F. Walter[3]

[1] University Grenoble Alpes, CNRS, IRD, IGE, Grenoble, France
[2] University Grenoble Alpes, CNRS, IRD, UGE, ISTerre, Grenoble, France
[3] Laboratory of Hydraulics, Hydrology and Glaciology, ETH Zürich, Zürich, Switzerland
[4] Aix Marseille Univ, CNRS, Centrale Marseille, LMA, France

**ABSTRACT**

Recent work in the field of cryo-seismology demonstrates that high frequency (>1 Hz) seismic waves provide key constraints on a wide range of glacier processes such as basal friction, surface crevassing or subglacial water flow. Establishing quantitative links between the seismic signal and the processes of interest however requires detailed characterization of the wavefield, which at high frequencies necessitates the deployment of large and particularly dense seismic arrays. Although dense seismic array monitoring has recently become increasingly common in geophysics, its application to glaciated environments remains limited. Here we present a dense seismic array experiment made of 98 3-component seismic stations continuously recording during 35 days in early spring 2018 on the Argentière Glacier, French Alps. The seismic dataset is supplemented with a wide range of complementary observations obtained from ground penetrating radar, drone imagery, GNSS positioning and in-situ measurements of basal glacier sliding velocities and subglacial water discharge. We present first results through conducting spectral analysis, template matching, matched-field processing and eikonal wave tomography. We report enhanced spatial resolution on basal

stick slip and englacial fracturing sources as well as novel constraints on the heterogeneous nature of the noise field generated by subglacial water flow and on the link between crevasse properties and englacial seismic velocities. We outline in which ways further work using this dataset could help tackle key remaining questions in the field.

## INTRODUCTION

The deployment of large and dense seismic arrays is becoming increasingly common in various geophysical contexts thanks to new technological developments of autonomous wireless seismographs and increased computational power. Spatially dense arrays enhance the characterization of high frequency (>1 Hz) body and surface waves propagating in the subsurface, such as for example in near-surface fault systems exhibiting hundreds to few tens of meters long structures (e.g., the Newport-Inglewood Fault, see Lin *et al.* (2013), and the San Jacinto Fault, see Roux *et al.* (2016)). The improved resolution provided by dense arrays increases the completeness of impulsive seismic event catalogs (Vandemeulebrouck *et al.*, 2013), thus allowing source spatio-temporal dynamics and subsurface structure to be studied in greater details (Meng and Ben-Zion, 2018; Chmiel *et al.*, 2019). Dense arrays also help to detect other sources of radiation (e.g. tremor and anthropogenic sources) compared to what is possible with single stations or regional networks (Inbal *et al.*, 2016; Li *et al.*, 2018; Meng and Ben-Zion, 2018). Despite its strong potential, dense array monitoring is still limited in the study of glaciers, although it could be used to address some of the key open questions in the field of glaciology.

Glaciers exhibit damage zones created by surface and/or basal crevasses (Walter *et al.*, 2015; Lindner *et al.*, 2019; Zhan, 2019; Sergeant *et al.*, 2020) as well as complex three dimensional

structures associated with firn/debris layers, bedrock topography or englacial water conduits (Cuffey and Paterson, 2010). These features are known to undergo large spatial and temporal changes and to play an important role in glacier dynamics and thermo-dynamics (Durand *et al.*, 2011; Scherler *et al.*, 2011; Gilbert *et al.*, 2020). However, conventional geophysical techniques such as radar sounders capable of resolving englacial structural features (e.g., Evans and Robin, 1966; Church *et al.*, 2019) are not suited for evaluating detailed spatial and temporal changes as well as their effects on the overall glacier behavior. Instead, active and passive surveys using dense seismic arrays may enable accurately monitoring these changes (e.g. using englacial seismic velocities, see Lindner *et al.* (2019) and Preiswerk *et al.* (2019)) and thus yield unprecedent constraints on glacier structure and temporal evolution.

Glaciers and ice sheets generate a large variety of seismic signals, from impulsive transients to emerging and sustained tremors (Podolskiy and Walter, 2016; Aster and Winberry, 2017). Impulsive arrivals from basal stick-slip events have been observed in numerous glaciological contexts (Weaver and Malone, 1979; Allstadt and Malone, 2014; Helmstetter, Nicolas, *et al.*, 2015; Lipovsky and Dunham, 2016; Lipovsky *et al.*, 2019; Walter *et al.*, 2020) and may yield crucial information on glacier basal motion, which exerts a primary control on glacier and ice-sheet dynamics and the associated eustatic sea level rise (Ritz *et al.*, 2015; Vincent and Moreau, 2016). The mechanisms giving rise to stick-slip sliding as well as its effect on large-scale ice flow, however, remain poorly constrained (Lipovsky *et al.*, 2019). Dense array monitoring could allow improving the detection of stick-slip events, yield more accurate inversions of locations and show if and how fast stick-slip asperities migrate.

77 Impulsive events from englacial fracturing are also commonly observed (Neave and Savage,
78 1970; Roux *et al.*, 2010; Mikesell *et al.*, 2012; Podolskiy *et al.*, 2018; Garcia *et al.*, 2019), and
79 may help elucidate the role of crevassing in iceberg calving, the disintegration of ice-shelves
80 and the occurrence of serac falls (Faillettaz *et al.*, 2008; Krug *et al.*, 2014; Lipovsky, 2018). The
81 improved detection and resolution provided by dense arrays could provide novel constraints
82 on crevasse depth and rupture propagation rates, which are needed to test models (van der
83 Veen, 1998; Weiss, 2004; Tsai and Rice, 2010) and thus better understand ice sheet integrity.
84
85 Recent seismic investigations have also reported widespread emergent and sustained tremor
86 signals generated by resonances in moulins or water-filled crevasses (Helmstetter, Moreau, *et*
87 *al.*, 2015; Roeoesli *et al.*, 2016; Aso *et al.*, 2017), subglacial water flow (Bartholomaus *et al.*,
88 2015; Eibl *et al.*, 2020; Lindner *et al.*, 2020; Nanni *et al.*, 2020) and subglacial sediment
89 transport (Gimbert *et al.*, 2016). The possibility to calculate physical characteristics of
90 subglacial water flow as well as of subglacial sediment transport from seismic tremor
91 observations (Tsai *et al.*, 2012; Gimbert *et al.*, 2014, 2016; Bakker *et al.*, 2020) is particularly
92 appealing. These processes play an important role in ice sliding speeds (Zwally *et al.*, 2002;
93 Schoof, 2010; Tedstone *et al.*, 2015) and bedrock erosion (Beaud *et al.*, 2016), and yet
94 hydraulic measurements at the ice bed are notoriously difficult, with traditional approaches
95 such as borehole techniques providing point measurements, only (e.g., Iken and Bindschadler,
96 1986; Iken *et al.*, 1993). Theoretical links between discharge, pressure regime, sediment
97 transport rates and geometry of the subglacial drainage system and seismogenic hydraulic
98 noise sources remain to be more fully tested and dense seismic arrays may provide the
99 necessary spatial extent and resolution for doing so.
100

Properly evaluating the knowledge gain that dense seismic arrays may provide to address the above-mentioned challenges requires (i) monitoring a glacier that gathers the processes of interest, (ii) deploying instrumentation that covers scales and durations over which significant changes operate, and (iii) acquiring complementary observations to test the seismically-derived findings and incorporate these into a wider glaciological context. Here we present data and first analysis from a 98 sensor array deployed over 35 days during early spring 2018 on an Alpine Glacier, the Argentière Glacier in the French Alps (Fig. 1). We also provide and analyze key complementary observations from Ground Penetrating Radar (GPR), drone imagery, Global Navigation Satellite System (GNSS) positioning and in-situ instrumentation of basal glacier sliding velocities and subglacial water discharge. We argue that the selected glacier, the time period of investigation as well as the completeness of the present dataset satisfies all of the three above-mentioned conditions. Through application of spectral analysis, template matching, matched-field processing and eikonal wave tomography, we demonstrate that use of the present dataset enhances spatial resolution of basal stick slip activity and near surface crevassing. We further provide novel constraints on the degree of heterogeneity of the seismic noise field generated by subglacial water flow and the variations of englacial seismic velocities. We finally outline how future work using this dataset could help overcome classical observational limitations and address key challenges in the field.

## EXPERIMENT DESIGN

### FIELD SITE

The Argentière Glacier is located in the Mont Blanc Massif (French Alps, 45°55’ N, 6°57’E, Fig. 1a) and is the second largest French glacier. It is about 10 km long, covers an area of about 12

126 $km^2$, extends from an altitude of 1700 m above sea level (a.s.l.) up to about 3600 m a.s.l. with
127 an equilibrium line altitude at about 2900 m a.s.l. (Vincent *et al.*, 2018). Over the past three
128 decades, glacier total mass balance has been negative (0.7 meter water equivalent loss per
129 year on average over the period 1976-2019), glacier snout has been retreating by several
130 hundreds of meters (815 m retreat between 1990 and 2019), glacier surface elevation has
131 decreased by several tens of meters and glacier surface velocities have decreased by about a
132 factor of two in the ablation zone (Vincent *et al.*, 2009). The upper part of the glacier is
133 constricted in a typical U-shaped narrow valley where ice sits on granite. The lower part of the
134 glacier is characterized by a sharper incised, V-shaped valley where ice sits on metamorphic
135 rocks (Vallon, 1967; Hantz and Lliboutry, 1983; Vincent *et al.*, 2009). The glacier generally
136 exhibits temperate bed conditions (Vivian and Bocquet, 1973), i.e. basal ice temperature is at
137 the pressure melting point and water flow occurs at the interface as a result of year-round
138 basal melt and summer surface melt (Cuffey and Paterson, 2010).
139
140 The monitored site is located in the lower part of the glacier (about 2 km from the glacier
141 front) and at about 2400 m a.s.l. (Fig. 1b). In this area the surface slope is gentle (1-2%) and
142 crevasses are restricted to an area of about 200 m from the glacier sides. The glacier flows at
143 a yearly average velocity of about 60 $m.yr^{-1}$ in its center, about half of which is due to sliding
144 at the ice-bed interface and the other half to internal ice deformation (Vincent and Moreau,
145 2016). Internal ice deformation likely occurs primarily through ice creep except near the
146 glacier sides where crevasses are large and potentially deep, such that englacial fracturing
147 could also play a role. A strong seasonality is observed in glacier dynamics, with summer
148 (typically May to September) velocities equal to about 1.5 times winter velocities (Vincent and

149 Moreau, 2016). This behavior is known to result from melt water input lubricating the ice-bed
150 interface and enhancing basal sliding (Lliboutry, 1959, 1968; Cuffey and Paterson, 2010).
151 Previous seismic observations at this site report various seismogenic sources associated with
152 surface and intermediate depth crevassing (Helmstetter, Moreau, *et al.*, 2015), basal stick-slip
153 (Helmstetter, Nicolas, *et al.*, 2015), subglacial water flow (Nanni *et al.*, 2020), and serac
154 instabilities in the glacier front (Roux *et al.*, 2008).
155
156 SEISMIC INSTRUMENTATION AND GEOPHYSICAL CHARATERISATION OF GLACIER STRUCTURE
157 AND DYNAMICS
158
159 **Seismic instrumentation**
160
161 Sensors of the dense seismic array (red dots in Fig. 1b) are Fairfield ZLand 3-component nodal
162 seismographs with a sampling frequency of 500 Hz (hereafter referred to as nodes). These
163 sensors have a low-corner cut-off frequency of 5Hz, a sensitivity of 76.7 $V.m^{-1}.s^{-1}$ (see Ringler
164 *et al.* (2018) for a detailed laboratory analysis of sensor response characteristics) and a typical
165 power autonomy of about 35 days. We deployed the nodes on 24 April 2018 when the glacier
166 was entirely covered by a snow layer of about 3 m thick. We placed the sensors about 40 m
167 apart from each other in the along-flow direction and about 50 m apart in the across-flow
168 direction in order to enable subwavelength analysis in the 4-50 Hz frequency range of interest.
169 Given that snow melt occurs at an average rate of 2-4 $cm.day^{-1}$ water equivalent at this
170 location (Vincent and Moreau, 2016), we decided to bury the nodes into snow about 30 cm
171 below the surface to ensure the sensors be (i) well coupled to their surroundings and
172 maintained levelled over a week-long time period until snow melt uncovered them and (ii)

shallow enough for the GNSS signal to pass through the snow layer and ensure proper reception for time synchronization. Given the limited melt that occurred over the first half of the monitoring period, we had to re-bury the sensors only once over the monitored period, on 11 May 2018. This strategy ensured that little data was lost due to melt-out-induced tilt.

We supplemented the seismic array with one three-component borehole seismic station placed at 5 m below the ice-surface (orange dot in Fig. 1b). This Geobit-C100 sensor was connected to a Geobit-SRi32L digitizer and provides higher sensitivity (1500 $V.m^{-1}.s^{-1}$), higher frequency sampling (1000 Hz) and a lower low-corner cut-off frequency (0.1 Hz) compared to the nodes. This seismic station is the same as the one used for the two-year long seismic study of Nanni *et al.* (2020).

**Recovery of surface and bed digital elevation models from structure from motion surveys and ground penetrating radar**

We construct a digital surface elevation model based on a drone geodetic survey that we conducted on September 5, 2018 when the glacier surface was snow free and crevasses could be identified. We used a senseFly eBee+ Unmanned Aerial Vehicle and acquired a total of 720 photos using the onboard senseFly S.O.D.A. camera (20 Mpx RGB sensor with 28 mm focal lens). We generate a digital elevation model of 10-cm resolution (see white contours in Fig. 1b) using differential Global Positioning System (GPS) measured ground control points (see green stars in Fig. 2a) and the Structure for Motion algorithm implemented in the software package Agisoft Metashape Professional version 1.5.2. A detailed description of the processing steps can be found in Brun *et al.* (2016) and Kraaijenbrink *et al.* (2016).

We calculate a crevasse map (black dots in Fig. 2a) based on the surface digital elevation model, which has been shown to be more reliable and precise than using optical/radar images (Foroutan *et al.*, 2019). We first apply a 2D highpass filter with a low cut-off wavelength of 10 m and then define any location with elevation lower than -50 cm as being part of crevasses. Finally, we apply a 2D median filter with a 1 by 1 m kernel in order to remove artifacts from boulders and moraines.

To establish a digital elevation model of the glacier bed we primarily use Ground Penetrating Radar (GPR) data acquired using a system of two transmitting and receiving 4.2 MHz antennas connected to a time triggered acquisition developed especially for glacial applications by the Canadian company Blue System Integration Ltd (Mingo and Flowers, 2010). The GPR signal processing consists of correcting for source time excitation. We use both dynamic corrections to reproduce a zero-incidence acquisition from data acquired with a 20 m offset between source and receiver (Normal Moveout correction) and static corrections to highlight elevation variations along a profile. We do so using a constant wave velocity of $0.168$ m.ns$^{-1}$ that is typical for ice (Garambois *et al.*, 2016). We then apply a [1-15 MHz] Butterworth band-pass filter followed by a squared time gain amplification to the signal in order to increase signal-to-noise ratio. We show an illustration of the processed GPR data in Fig. 2b, where the direct air-wave first arrival is followed by a large reflectivity V-shape pattern reaching $3000$ ns around the center of the profile. This latter profile corresponds to the ice/bedrock interface, although its apparent shape is biased by reflections off the closest point on the ice-bed interface rather than off the bed portion directly below the instrument. We correct for this bias by applying a frequency-wavenumber Stolt migration technique (Stolt, 1978) and convert time into distance

using the constant wave velocity of $0.168$ m.ns$^{-1}$. We note that prior to migration we add null traces (i.e. with null amplitudes) in places where harsh glacier surface conditions (mainly crevasses) prevented us from acquiring data. As illustrated in Fig. 2c the migration process is effective in correcting the artefacts due to the geometrical variation of the interface along the profile, which now appears smooth and continuous. We then pick the ice-bed reflection (yellow line in Fig. 2c) over all GPR profiles, such that a three-dimensional bed DEM can be reconstructed.

We reconstruct a three-dimensional bed DEM over a larger area than that covered by GPR surveys by incorporating additional constraints like glacier edge elevation as measured from drone imagery (blue area in Fig. 2a) and bed elevations obtained through rock drilling to the ice-bed interface from bedrock excavated tunnels located further down-glacier (purple area in Fig. 2a). Furthermore, we interpolated all data using a kriging method onto a 10 by 10 m grid. From different first onset pickings we estimate that the recovered depth uncertainty is of about 5 m below the seismic array and likely on the order of a few tens of meters outside of the array where observations are sparser.

In Fig. 2a we show the ice thickness map (using 25-m bin contours) as reconstructed based on subtracting the bed DEM from the surface DEM. The glacier bed exhibits a gently dipping valley, with a maximum ice thickness of about 255 m at the center of the seismic array. Glacier thickness decreases relatively sharply on the glacier margins where surface crevasses are observed. We also observe that bed elevation significantly increases down glacier, which results in a decrease by more than 150 m in glacier thickness (Fig. 2d). Beyond these generic characteristics we identify two interesting reflectivity features in the migrated GPR images

245 (yellow ellipses in Fig. 2c) that correspond to localized scattering observed near the surface
246 and a large reflectivity pattern observed just above the deepest portion of the interface. The
247 near surface scattering feature could be caused by deep crevasses, and the deeper feature
248 could be caused by englacial and/or subglacial water conduits as recently proposed by Church
249 *et al.* (2019), who made similar GPR observations in a temperate glacier and were able to
250 bolster their interpretation with in-situ borehole observations.
251
252 **Meteorological and water discharge characteristics**
253
254 We use air temperature and precipitation measurements obtained at a 0.5 h time step with
255 an automatic weather station maintained by the French glacier-monitoring program
256 GLACIOCLIM (Les GLACIers un Observatoire du CLIMat; https://glacioclim.osug.fr/), which is
257 located on the moraine next to the glacier at 2400 m a.s.l. (green diamond in Fig. 1b).
258 Precipitation is measured with an OTTPluvio weighing rain gauge. Subglacial water discharge
259 is monitored at a 15 min time step in tunnels excavated into bedrock by the Emossons
260 hydraulic power company, which are located 600 m downstream of the array center (at 2173
261 m a.s.l.) near the glacier ice fall (see blue star in Fig. 1b).
262
263 Temperature generally increases over the instrumented period, from a multi-daily average of
264 about 0° C at the beginning of the measurement period to about 5 °C at the end (Fig. 3a). This
265 drives the general increase in water discharge, which varies from few tenths of $m^3.s^{-1}$ to
266 several $m^3.s^{-1}$ over the period. Episodic rain events also occur during the instrumented period,
267 but have little to no effect on subglacial discharge likely as a result of the snow cover acting as
268 a water storage buffer (Fountain and Walder, 1998).

**Glacier dynamics instrumentation and general features**

We evaluate changes in glacier dynamics over the instrumented period by means of two observational methods. The first one is unique to the present site, and consists of basal sliding velocity measurements made continuously in the down glacier serac fall area (see red star in Fig. 1b) by means of a bicycle wheel placed directly in contact with the basal ice at the extremity of an excavated tunnel (Vivian and Bocquet, 1973; Moreau, 1999). The wheel is coupled with a potentiometer that retrieves its rotation rate, which is then recorded digitally and converted back to a sliding velocity at a 1-s sampling time with a displacement increment resolution of 0.07 mm. The second type of measurements consists of 4 glacier surface and 1 reference bedrock GNSS stations (yellow stars in Fig. 1b) of type Leica GR25 acquiring the GNSS signals every second. This temporary array is supplemented by a permanent ARGR GNSS station from the RESIF-RENAG network (http://renag.resif.fr) on the bedrock close to the glacier 3 km uphill (yellow star in Fig. 1a). The GNSS antennas on the glacier are installed on 8-m long aluminum masts anchored 4-m deep in the ice and thus emerging about a meter above the snow surface at the beginning of the measurement period. The temporary station placed next to the glacier side provides a reference for validating kinematic GNSS processing approaches, evaluating station positions from every single set of GNSS signal recordings (i.e. every second, as opposed to static processing, which cumulates GNSS signals over a much longer time). We conduct such kinematic processing using the TRACK software ((Herring *et al.*, 2018), http://geoweb.mit.edu/gg/docs.php). Our processing chain includes the on-line tool SARI (https://alvarosg.shinyapps.io/sari/) for the removal of outliers that arise from low satellite coverage in the glacier valley and to perform a de-trend and re-trend analysis to

293 estimate and correct for offsets due to manual antenna mast shortening as snow melt
294 progresses. We also correct for multi-path effects induced by GNSS signal reflections from the
295 ground, although we find that those are attenuated by the combination of GPS and GLONASS
296 signals thanks to their different sidereal periods (~24 h for GPS and ~8 days for GLONASS). We
297 finally calculate position time series at a 30-s time step sufficient to capture glacier dynamics
298 and subsequently evaluate three-dimensional velocities by the linear trends of the position
299 components. The horizontal velocity is calculated as $v_h = \sqrt{v_N^2 + v_E^2}$ where $v_N$ and $v_E$ are
300 the North and East components, respectively.
301
302 To facilitate comparison of basal sliding and surface velocity here we smooth both timeseries
303 at a 36-hr timescale (Fig. 3b), since daily down to sub-daily fluctuations in basal sliding
304 velocities are largely affected by unconstrained variations in the local ice roughness in contact
305 with the wheel, as for example, when an entrained rock passes over the wheel. Although basal
306 sliding velocity is to be lower than surface velocity, here both quantities have similar absolute
307 values because the sliding velocity is measured at a place where the glacier is much steeper
308 (25% slope as opposed to 1-2%) and thus driving stress is much larger than at the GNSS
309 locations. We observe an increase in basal sliding velocity from 4.5 mm/h to more than 6
310 mm/h at the very beginning of the monitored period. Such an acceleration is commonly
311 observed in spring on alpine glaciers (Iken and Bindschadler, 1986; Mair *et al.*, 2002; Vincent
312 and Moreau, 2016) and is known to correspond to water pressurization caused by an increase
313 in water input at the bed due to surface melt water supply, which causes the reduction of
314 friction and thus the enhancement of sliding (Lliboutry, 1959, 1968; Iken, 1981; Schoof, 2005;
315 Gagliardini *et al.*, 2007). This acceleration is not seen in the GNSS observations, which could
316 be due to the glacier seasonal acceleration occurring earlier at this location. We also observe

one major acceleration event in the location of the dense seismic array occurring between 4 May and 8 May 2018 likely due to the large concomitant increase in water discharge (see blue line in Fig. 3a) causing basal water pressurization (Cuffey and Paterson, 2010).

## FIRST RESULTS

### SEISMIC NOISE CHARACTERISTICS

We investigate the spatial and temporal variability of seismic power $P$ (in dB) across a wide range of frequencies by applying Welch's method (Welch, 1967) over 4 seconds-long vertical ground motion timeseries (with 50 % overlap) prior to averaging power (in the decibel space) over 15 minutes-long time windows. This two-step strategy allows limiting the influence of impulsive events (which are studied in more details in the next sections) on the seismic power while enhancing that of the continuous background noise (Bartholomaus *et al.*, 2015; Nanni *et al.*, 2020). In Fig. 4 we present 1-100 Hz spectrograms (i.e. seismic power at any given frequency and time) over the first half of the instrumented period (15 April to 14 May 2018) together with timeseries of 2-20 Hz frequency median seismic power at five different stations of the array, four stations located on the four array sides and one located in the array center (see node numbers in Fig. 1b and Fig. S1 for spectrograms across all stations and over the entire frequency range and experimental period). Time periods when sensors tilted beyond their specifications (and thus were no longer deemed functional) as a result of snow melt causing them to be no longer buried are manifested by drastically reduced seismic power across the whole frequency range (see node 6 from 8 May to 11 May 2018). Fortunately,

sensor tilt only occurred at a small number of seismic stations (11 out of 98) and during a restricted time duration (less than 2 days on average, see Fig. S1). We also observe that spectrograms do not undergo significant change from prior to after sensor reinstallation on 11 May 2018. This suggests that these are not significantly affected by potential changes in sensor coupling to snow, which is pleasant given that a previous study found that coupling can strongly affect nodes recorded signals (Farrell *et al.*, 2018).

All stations generally experience similar multi-day (e.g. four days' average, see black lines in Fig. 4) variations in seismic power that are highly correlated with multi-day discharge variations, although seismic power precedes discharge variations by about a day or two. The likely reason is that seismic power is controlled by the hydraulic pressure gradient, which is highest during periods of rising discharge (Gimbert *et al.*, 2016; Nanni *et al.*, 2020). Although shorter term (e.g. diurnal) variations in seismic power are also similar across stations when discharge is low (from 24 April to 28 April and from 30 April to 4 May) and anthropogenic noise dominates (Nanni *et al.*, 2020), the picture is different at higher discharges when seismic power is dominated by subglacial water flow (Nanni *et al.*, 2020). On 29 April and from 5 May to 10 May seismic power exhibits pronounced (up to 10 dB) and broad frequency (1-100 Hz) short time scale (sub-diurnal to diurnal) variations that are particularly marked at certain stations (e.g. node 6 (Fig. 4a), node 44 (Fig. 4c) and node 50 (Fig. 4d)) and not at others (e.g. node 38 (Fig. 4b) and 95 (Fig. 4e)). We also observe that at certain stations seismic power appears to be continuously or intermittently enhanced within narrow frequency bands. For instance node 38 systematically presents higher seismic power above 20 Hz. These discrepancies suggest that measurements of ground motion amplitude are sensitive to heterogenous and intermittent subglacial water flow, although certain features discussed

here could be due to extraneous noise sources associated with sensor coupling (Farrell *et al.*, 2018), to localized sources other than subglacial fluid flow or to site effects.

## DETECTING AND LOCATING BASAL STICK SLIP IMPULSIVE EVENTS USING TEMPLATE MATCHING

We detect high-frequency (>50 Hz) basal stick-slip events using template matching. This follows a two-step analysis as in Helmstetter *et al.* (2015). We first build a catalog of events through applying a short-term-average over long-term-average (STA/LTA) detection method (Allen, 1978) to the continuous high-pass filtered signal (>20 Hz) using a STA time window of 0.1 s and a LTA time window of 1 s. We identify an event when the STA/LTA ratio exceeds a factor of 2. We then manually select all events with short duration (<0.2 s) and high average frequency (>50 Hz) and define groups of events referred to as clusters when their correlation with each other exceeds 0.8. For each cluster, we compute the average waveform to define its "template" signal (using a time window of 0.25 s). We take the sum of seismograms normalized by their peak amplitude and weighted by the square correlation between each event and the template event, iterating this procedure several times until convergence. We visually check that events present distinct P and S wave arrivals and use a polarization analysis to ensure that they are not associated with surface waves (Fig. 5a). We then use the template matching filter method (Gibbons and Ringdal, 2006) to further detect smaller amplitude events not picked with the above strategy but exhibiting a correlation higher than 0.5 with the template signal.

We first conduct the analysis using the borehole station ARG, which has a higher sensor sensitivity, signal-to-noise and sampling rate compared to the nodes. We identify 31 active clusters during the dense array experiment. Interestingly, these clusters constitute a large part of the 46 clusters identified on a much longer period (from December 2017 to June 2018, using the borehole sensor which ran almost continuously, see Fig. 6). Although the amplitude of these signals varies strongly through time (from $1 \cdot 10^{-7}$ m.s$^{-1}$ to $4 \cdot 10^{-6}$ m.s$^{-1}$ Fig. 6a), waveform characteristics remain strikingly similar (Fig. 6b and 6c). All 46 identified clusters exhibit similar characteristics to that shown in Fig. 6, and their activity does not appear to be temporally correlated with each other, nor with external drivers related to meteorology, hydrological or glacier dynamics.

We also apply the template matching algorithm on a subset of 10 nodes covering the whole study area, using the same 31 clusters as previously identified using station ARG. At each time step we compute the correlation coefficient between each template signal and the continuous signal averaged over all nodes and all components (using a time window of 0.35 s instead of 0.25 s in order to match signal duration at all selected nodes). The large number of sensors allows us to lower the correlation threshold from 0.5 to 0.2 while reducing the number of false detections. Indeed, events belonging to different clusters with very different locations can end up being correlated above the detection threshold when using one station, while using several stations this scenario is much more unlikely. We detect 79% more events using the nodes compared to using the station ARG. The newly detected events are mostly smaller amplitude events. Most (83%) of the events detected using ARG are also detected using the nodes. This shows that increasing the number of sensors allows detecting more events and reducing the number of false detections despite signal-to-noise ratio and sampling rate not being optimum.

We determine the position of the 31 identified clusters by first manually picking on each node the P and S arrival times associated with the event in each cluster that is associated with the largest correlation with the template event, and then inverting for the location of each event and the associated P and S wave velocities assuming velocities are homogeneous and identical for all events. We only consider first arrivals that are usually geometrically predicted to be direct (as opposed to refracted) waves for most sensors and most events. Assuming a simple 1D velocity model with $V_P$=3620 m/s in the ice and $V_P$=4300 m/s in the bedrock (see Fig 10b) and a glacier thickness of 200 m, the direct wave is faster for epicentral distances shorter than 306 m. Moreover, even when the refracted wave is faster, it is usually less impulsive and has a smaller amplitude than the direct wave. We estimate P and S wave velocities using a grid search inversion with a step of 10 m.s$^{-1}$ and the Nonlinloc software (Lomax *et al.*, 2000) to locate clusters. We assume a standard error of arrival times of $2 \cdot 10^{-3}$ s for P waves, $4 \cdot 10^{-3}$s for S waves and of $3.5 \cdot 10^{-3}$ s for calculated travel times. We can see in Fig. 5a that the picked arrival times (black circles) are consistent with the computed travel times (green lines). The root-mean-square error for this event is 2.4 ms, which corresponds to about one sample (2 ms).

We show the locations of basal icequakes versus depth in an average transverse section in Fig. 7a and on a two-dimensional map in Fig. 8. They are mainly located in the down-glacier part of the array and in the central part of the glacier or near the right side, while there is no event observed towards the left side. Icequake depths range between 80 m and 285 m, and are in good agreement with the bedrock topography estimated from the radar profiles. Uncertainty on absolute source depth is on the order of 10 m (see errorbars in Fig. 7a), and the estimated

seismic wave velocities of $V_P$=3620 m.s$^{-1}$ and $V_S$=1830 m.s$^{-1}$ (Fig. 7b) are in good agreement with velocities measured on other alpine glaciers (Podolskiy and Walter, 2016). $V_S$ is much better constrained by the data compared to $V_P$ (Fig. 7b).

## SYSTEMATIC LOCATION OF EVENTS USING MATCHED-FIELD PROCESSING

Contrary to in the previous section where a priori constraints on waveform characteristics and wave velocity are used to target basal stick-slip events, we next test location of a wide range of seismic events generated by impulsive or emergent sources with no a priori knowledge on waveform characteristics and minimal a priori knowledge on medium properties. The rationale is that the limited a-priori knowledge for source identification is balanced by the high spatial and temporal resolution provided by array processing techniques, which may provide spatial or temporal characteristics facilitating source identification (Vandemeulebrouck *et al.*, 2013; Chmiel *et al.*, 2019).

We conduct Matched-Field Processing (MFP), which consists of recursively matching a synthetic field of phase delays between sensors with that obtained from observations using the Fourier transform of time-windowed data. We obtain the synthetic field from a source model with a frequency-domain Green's function that depends on 4 parameters, which are the source spatial coordinates $x$, $y$ and $z$ and the medium phase speed $c$. MFP output is normalized to range from 0 to 1 with higher values corresponding to better matches between modelled and observed signal phases, and therefore a higher confidence in true source location. Here we use a spatially homogeneous velocity field within the glacier, which the advantage of a fast-analytical computation, although it also results in a higher degree of

460 ambiguity between $z$ and $c$. Contrary to classical beamforming techniques in which a planar
461 wave front is often assumed, our MFP approach considers spherical waves and allows locating
462 sources closer to and within the array. To build a large catalog of events, we apply MFP over
463 short time windows of 1-s with 0.5-s overlap, across 16 frequency bands of ±2 Hz width equally
464 spaced from 5 to 20 Hz and over the entire study period. Calculating source locations over
465 such a large number of windows requires minimizing computational cost. We do so by using
466 a minimization algorithm that relies on the downhill simplex search method (Nelder-Mead
467 optimization) of Nelder and Mead (1965) and Lagarias *et al.* (1998) instead of using a multi-
468 dimensional grid search approach. As the exploration of the solution space is characterized by
469 a certain level of randomness, we maximize the likelihood that our minimization technique
470 finds a global minima and thus the dominant source over the considered time window through
471 (i) starting the optimized algorithm from a set of 29 points located at a depth of 250 m inside
472 and near the array (see black crosses in Fig. 9d) with a starting velocity $c$=1800 m.s$^{-1}$ and (ii)
473 taking the highest MFP output out of the 29 inversions found after convergence.
474
475 In Fig. 9b,c we present two examples of events located inside and outside the array and
476 associated with a high MFP output of 0.92. The half-size of the focal spot in the MFP output
477 field gives a measure of the location uncertainty (Rost and Thomas, 2002), which is about 10
478 m for events located inside the array and can increase up to 40 m when for events up to 100
479 m away from the array edges. Gathering all sources over one continuous day of record, we
480 find that the associated MFP output distribution exhibits a heavy tail towards high values (red
481 area in Fig. 9a for an example at 13 Hz). Such a heavy tail is not obtained for a random field,
482 in which case MFP output exhibits a distribution shifted towards almost one order of
483 magnitude lower values. This suggests that most identified sources correspond to real and

detectable seismic events. Well resolved seismic events with MFP outputs higher than 0.8 are located near the surface and delineate crevasse geometries, such that they likely correspond to englacial fracturing (red dots in Fig. 8). Few (less than one percent) of these events are however located outside of the glacier and likely correspond to rock falls. Typical waveforms associated with englacial fracturing events are dominated by surface waves arrivals (Fig. 5b), although P waves arrivals as well as arrivals showing hyperbolic moveout (black arrows in Fig. 5b) are also distinguishable. Although P waves arrivals associated with surface crevassing events are not commonly observed (Walter *et al.*, 2009; Helmstetter, Moreau, *et al.*, 2015), their observation here may result from improved detection thanks to the dense seismic array. Arrivals showing hyperbolic moveout likely correspond to reflected waves at the glacier/bedrock interface.

## USING EVENT CATALOGS FOR STRUCTURE INVERSION

Dense-array techniques for seismic imaging often involve interferometry analysis on continuous seismic noise. Such techniques however require an equipartitioned wavefield inherited directly from homogenously distributed noise sources and/or indirectly from sufficiently strong scattering (Lobkis and Weaver, 2001; Fichtner *et al.*, 2019). These conditions strongly limit the applicability of such techniques on glaciers where sources are often localized and waves in ice are weakly scattered (Sergeant *et al.*, 2020). An alternative way is to use localized and short-lived sources with known positions (Walter *et al.*, 2015) as those previously identified using our systematic MFP technique, which are numerous and more evenly distributed in space (Fig. 8).

508

509 We consider the catalog of sources associated with MFP outputs larger than 0.6, located near
510 the surface (z<10m) and close to the array (within a radius of 400 m from the array center).
511 With these criteria our catalog includes about $10^6$ sources gathered over the 35 days of
512 continuous recordings. In order to further demonstrate that our MFP calculations yield
513 reliable velocities (i.e. the ambiguity between $z$ and $c$ is limited for these sources), we use the
514 velocities given from our MFP calculation (which for shallow events recover the dominant
515 surface waves) to construct dispersion curves, as opposed to classical f-k analysis (Capon,
516 1969). We infer surface wave phase velocity at each frequency between 3.5 Hz and 25 Hz by
517 fitting a Gaussian function to the probability density distributions of velocities in each
518 frequency bin, and taking the center of the Gaussian function as the most representative
519 velocity in that frequency bin (see Fig. 10a (inset) for an example at 13 Hz). We note that the
520 presently constructed dispersion curve is similar to the one that would be obtained using a
521 classical f-k analysis (not shown). We find that surface wave velocity increases gently from
522 1560 m.s$^{-1}$ to 1630 m.s$^{-1}$ as frequency decreases from 25 Hz down to 7 Hz, and then increases
523 sharply up to 2300 m.s$^{-1}$ as frequency decreases down to 3.5 Hz. These observations can be
524 reproduced using a three-layer one-dimensional elastic model (using the Geopsy package,
525 Wathelet *et al.* (2020)) that incorporates a gentle velocity increase (from 1670 to 1720 m.s$^{-1}$
526 for $V_S$) at 40 m depth and a drastic velocity increase (from 1720 to 2800 m.s$^{-1}$ for $V_S$) located
527 between 200 and 220 m depth (Fig. 10b). These values were obtained by trial and error tests.
528 The slightly slower velocities and density within the first 40-m deep layer may be due to
529 surface crevasses, and are consistent with surface events being associated with smaller P wave
530 velocities than those associated with stick-slip events at the ice/bedrock interface (Fig. 5). The

531 200- to 220-m deep drastic discontinuity results from the ice/bedrock interface, consistent
532 with the radar-derived average glacier thickness beneath the seismic network (Fig. 2a).
533
534 We go one step further and perform two-dimensional surface wave inversions from eikonal
535 wave tomography (Roux *et al.*, 2011; Lin *et al.*, 2013; Mordret *et al.*, 2013). We first extract
536 ~200,000 Rayleigh wave travel times using the best (associated with MFP outputs larger than
537 0.9) seismic events and then perform a simple linear inversion for the slowness (starting from
538 a homogeneous initial model with a phase velocity of 1580 $m.s^{-1}$, see Fig. 10a) assuming
539 straight rays as propagation paths and an *a-priori* error covariance matrix that decreases
540 exponentially with distance over 10 m. The weight of the spatial smoothing is chosen at the
541 maximum curvature of the standard trade-off analysis (L-curve) based on the misfit value
542 (Hansen and O'Leary, 1993), and the inversion produces a residual variance reduction of ~98%
543 relative to the arrival times for the homogeneous model. In Fig. 8 we show the Rayleigh wave
544 phase velocity maps obtained as a result of the travel-time inversion on a regular horizontal
545 grid with steps of 5 m and using 13-Hz Rayleigh waves, which have largest sensitivity between
546 20 m and 60 m depth (Fig. 10c) according to kernel sensitivity computations performed on the
547 three layer elastic model (Fig. 10b) using the code of Herrmann (2013). We observe that
548 locations with higher crevasse density are generally associated with lower phase velocities, as
549 observed in the left glacier side and in the down glacier part of the array. This observation is
550 however not systematic, since high velocities are also observed in the right glacier side and in
551 the up glacier part of the array where crevasses are also present. This could be explained by
552 shallower crevasses or by crevasse orientations, which affect different wave propagation
553 directions in these regions. This latter potential source of bias could be investigated by

554 explicitly accounting for anisotropy in the tomography inversion scheme (Mordret *et al.*,
555 2013).
556
557
558 **DISCUSSION**
559
560 INTERPRETING SPATIAL AND TEMPORAL VARIATIONS IN GROUND MOTION AMPLITUDES
561
562 Although our seismic array observations generally exhibit spatially homogenous multi-day
563 changes in seismic power, there exist specific times when changes in seismic power are
564 spatially heterogeneous (Fig. 4). A surprising observation is that these heterogeneous changes
565 are observed down to the lowest frequencies (3 to 10 Hz) associated with wavelengths larger
566 than the inter-station spacing, such that the observed spatial heterogeneity is unlikely solely
567 caused by wave attenuation. It remains to be investigated as to which processes mainly cause
568 the observed spatial variability in seismic power. Punctual sources identified from the MFP
569 analysis could be used to investigate the respective control of wave attenuation, wave
570 scattering and site effects on amplitude field heterogeneity and its potential dependency on
571 site attributes like crevasse density, glacier thickness or snow layer thickness. Full waveform
572 modelling combined with wave polarity analysis could also be conducted in order to further
573 understand how wave focusing in the near field domain as well as source heterogeneity and
574 directivity may cause heterogenous amplitude wavefields. Incorporating these constraints
575 into an improved model describing the control of both source and wave propagation physics
576 on the seismic wave amplitude field (Gimbert *et al.*, 2016) could allow using our dense array

observations to infer the spatial variability in subglacial water flow parameters such as subglacial channel size and pressure.

## PHYSICS OF STICK SLIP EVENTS

We demonstrate that dense array observations provide enhanced resolution on stick-slip motion. Applying template matching on an array of sensor as opposed to on a single station enables detecting many more events within clusters. Using the whole array for location inversions also allows significantly reducing location uncertainties. Future studies may focus on applying template matching across all sensors of the array in order to detect and locate more events within clusters and potentially more clusters. With our present analysis we find that events are all located in the down-glacier part of the array and in the central part of the glacier or near the right side, while there is no event observed towards the left side (Fig. 7 and 8). This provides further observational support that specific bed conditions (e.g. water pressure, bed shear stress, bed roughness, bed topography, carried sediments) are necessary for these events to occur (Zoet *et al.*, 2013; Lipovsky *et al.*, 2019). Further insights into the physics controlling the spatio-temporal dynamics of these events could be gained by performing relative event location within each cluster using double-differences (Waldhauser and Ellsworth, 2000) instead of simply inferring single cluster locations as presently done. These improvements could allow identifying whether or not stick-slip asperities migrate.

## USING MFP TO RETRIEVE SOURCES AND STRUCTURAL PROPERTIES

Systematic MFP analysis with adequate parametrization opens a route to continuous, automatic, and statistics-based monitoring of glaciers. A wide diversity of seismic sources may be identified and studied separately with this technique by scanning through different values of MFP outputs. High MFP outputs may be used to study the dynamics of crevasse propagation with particularly high spatio-temporal resolution. Such observations may allow to better understand the underlying mechanisms associated with crack propagation, in particular through providing an opportunity to better bridge the gap between laboratory and theoretical material physics of crack propagation (van der Veen, 1998; Weiss, 2004) and crevasse propagation under realistic glacier conditions in which water is expected to play an important role (van der Veen, 2007). Lower MFP outputs may be used to locate spatially distributed sources generating coherent signals over only a limited spatial extent. These distributed sources may include tremor sources (e.g. water flow) or various glacier features (e.g. crevasses, englacial conduits) acting as scatterers. One could also combine MFP with eigenspectral decomposition to reveal weaker noise sources that would otherwise be hidden within the background noise (Seydoux *et al.*, 2016). Additional constraints for seismic imaging may also be provided through identifying specific events generating indirect arrivals of particular interest for structural analysis, such as in bed-refracted waves shown in Fig. 5 (black arrows).

## SUMMARY

We present a dense seismic array experiment made of 98 3-component seismic stations continuously recording during 35 days in early spring 2018 on the Argentière Glacier, French Alps. The seismic dataset is supplemented by complementary observations obtained from

ground penetrating radar, drone imagery, GNSS positioning and in-situ instrumentation of basal glacier sliding velocities and subglacial water flow discharge. We show that a wide range of glacier sources and structure characteristics can be extracted through multiple seismic processing techniques such as spectral analysis, template matching, matched-field processing and eikonal wave tomography. Future studies focusing more specifically on each aspect of the herein presented observations may yield novel quantitative insights into spatio-temporal changes in glacier dynamics and structure.

## DATA AND RESOURCES

Raw seismic data can be found at:

Roux, P., Gimbert, F., & RESIF. (2021). *Dense nodal seismic array temporary experiment on Alpine Glacier of Argentière (RESIF-SISMOB)* [Data set]. RESIF - Réseau Sismologique et géodésique Français. https://doi.org/10.15778/RESIF.ZO2018 (see also link http://seismology.resif.fr/#NetworkConsultPlace:ZO%5B2018-01-01T00:00:00_2018-12-31T23:59:59%5D).

Processed data used in this paper can be found at:

- https://doi.org/10.5281/zenodo.3701519 for meteorological, subglacial water flow discharge and glacier sliding speed data
- https://doi.org/10.5281/zenodo.3971815 for bed thickness, surface elevation, nodes positions, crevasses positions, surface velocity, noise PSDs, event occurrences and locations derived from template matching for stick-slip events and MFP for englacial fracturing events
- https://doi.org/10.5281/zenodo.3556552 for drone orthophotos

## ACKNOWLEDGEMENTS

This work has been supported by a grant from Labex OSUG (Investissements d'avenir – ANR10 LABX56). IGE and IsTerre laboratories are part of Labex OSUG (ANR10 LABX56). Complementary funding sources have also been provided for instrumentation by the French "GLACIOCLIM (Les GLACIers comme Observatoire du CLIMat)" organization and by l'Agence Nationale de la recherche through the SAUSSURE (, ANR-18-CE01-0015) and SEISMORIV (ANR-17-CE01-0008) projects. We thank C. Aubert, A. Colombi, L. Moreau, L. Ott, I. Pondaven, B. Vial, L. Mercier, O. Coutant, L. Baillet, M. Lott, E. LeMeur, L. Piard, S. Escalle, V. Rameseyer, A.

Palanstjin, A. Wehrlé and B. Urruty for their help in the field, as well as Martin, Fabien and Christophe for mountain guiding the group.

## REFERENCES

Allen, R. V. (1978). Automatic earthquake recognition and timing from single traces, *Bulletin of the Seismological Society of America* **68**, no. 5, 1521–1532.

Allstadt, K., and S. D. Malone (2014). Swarms of repeating stick-slip icequakes triggered by snow loading at Mount Rainier volcano, *Journal of Geophysical Research: Earth Surface* **119**, no. 5, 1180–1203, doi: 10.1002/2014JF003086.

Aso, N., V. C. Tsai, C. Schoof, G. E. Flowers, A. Whiteford, and C. Rada (2017). Seismologically Observed Spatiotemporal Drainage Activity at Moulins, *Journal of Geophysical Research: Solid Earth* **122**, no. 11, 9095–9108, doi: 10.1002/2017JB014578.

Aster, R. C., and J. P. Winberry (2017). Glacial seismology, *Reports on Progress in Physics* **80**, no. 12, 126801, doi: 10.1088/1361-6633/aa8473.

Bakker, M., F. Gimbert, T. Geay, C. Misset, S. Zanker, and A. Recking (2020). Field Application and Validation of a Seismic Bedload Transport Model, *Journal of Geophysical Research: Earth Surface* **125**, no. 5, e2019JF005416, doi: 10.1029/2019JF005416.

Bartholomaus, T. C., J. M. Amundson, J. I. Walter, S. O'Neel, M. E. West, and C. F. Larsen (2015). Subglacial discharge at tidewater glaciers revealed by seismic tremor, *Geophys. Res. Lett.* **42**, no. 15, 2015GL064590, doi: 10.1002/2015GL064590.

Beaud, F., G. E. Flowers, and J. G. Venditti (2016). Efficacy of bedrock erosion by subglacial water flow, *Earth Surface Dynamics* **4**, no. 1, 125–145, doi: https://doi.org/10.5194/esurf-4-125-2016.

Brun, F., P. Buri, E. S. Miles, P. Wagnon, J. Steiner, E. Berthier, S. Ragettli, P. Kraaijenbrink, W. W. Immerzeel, and F. Pellicciotti (2016). Quantifying volume loss from ice cliffs on debris-covered glaciers using high-resolution terrestrial and aerial photogrammetry, *Journal of Glaciology* **62**, no. 234, 684–695, doi: 10.1017/jog.2016.54.

Capon, J. (1969). High-resolution frequency-wavenumber spectrum analysis, *Proceedings of the IEEE* **57**, no. 8, 1408–1418, doi: 10.1109/PROC.1969.7278.

Chmiel, M., P. Roux, and T. Bardainne (2019). High-sensitivity microseismic monitoring: Automatic detection and localization of subsurface noise sources using matched-field processing and dense patch arraysHigh-sensitivity microseismic monitoring, *Geophysics* **84**, no. 6, KS211–KS223, doi: 10.1190/geo2018-0537.1.

Church, G., A. Bauder, M. Grab, L. Rabenstein, S. Singh, and H. Maurer (2019). Detecting and characterising an englacial conduit network within a temperate Swiss glacier using active seismic, ground penetrating radar and borehole analysis, *Annals of Glaciology* **60**, no. 79, 193–205, doi: 10.1017/aog.2019.19.

Cuffey, K. M., and W. S. B. Paterson (2010). *The Physics of Glaciers*, 4th edn, Butterworth-Heinemann, Burlington, Burlington, MA, USA.

Durand, G., O. Gagliardini, L. Favier, T. Zwinger, and E. le Meur (2011). Impact of bedrock description on modeling ice sheet dynamics, *Geophysical Research Letters* **38**, no. 20, doi: 10.1029/2011GL048892.

Eibl, E. P. S., C. J. Bean, B. Einarsson, F. Pàlsson, and K. S. Vogfjörd (2020). Seismic ground vibrations give advanced early-warning of subglacial floods, 1, *Nature Communications* **11**, no. 1, 2504, doi: 10.1038/s41467-020-15744-5.

Evans, S., and G. de Q. Robin (1966). Glacier Depth-Sounding from the Air, 5039, *Nature* **210**, no. 5039, 883–885, doi: 10.1038/210883a0.

709 Faillettaz, J., A. Pralong, M. Funk, and N. Deichmann (2008). Evidence of log-periodic
710 oscillations and increasing icequake activity during the breaking-off of large ice masses,
711 *Journal of Glaciology* **54**, no. 187, 725–737, doi: 10.3189/002214308786570845.
712 Farrell, J., S.-M. Wu, K. M. Ward, and F.-C. Lin (2018). Persistent Noise Signal in the
713 FairfieldNodal Three-Component 5-Hz Geophones, *Seismological Research Letters* **89**, no. 5,
714 1609–1617, doi: 10.1785/0220180073.
715 Fichtner, A., L. Gualtieri, and N. Nakata (Editors) (2019). Theoretical Foundations of Noise
716 Interferometry, in *Seismic Ambient Noise*, Cambridge University Press, Cambridge, 109–143,
717 doi: 10.1017/9781108264808.006.
718 Foroutan, M., S. J. Marshall, and B. Menounos (2019). Automatic mapping and
719 geomorphometry extraction technique for crevasses in geodetic mass-balance calculations at
720 Haig Glacier, Canadian Rockies, *Journal of Glaciology* **65**, no. 254, 971–982, doi:
721 10.1017/jog.2019.71.
722 Fountain, A. G., and J. S. Walder (1998). Water flow through temperate glaciers, *Reviews of*
723 *Geophysics* **36**, 299–328, doi: 10.1029/97RG03579.
724 Gagliardini, O., D. Cohen, P. Råback, and T. Zwinger (2007). Finite-element modeling of
725 subglacial cavities and related friction law, *J*. *Geophys*. *Res*. **112**, no. F2, F02027, doi:
726 10.1029/2006JF000576.
727 Garambois, S., A. Legchenko, C. Vincent, and E. Thibert (2016). Ground-penetrating radar and
728 surface nuclear magnetic resonance monitoring of an englacial water-filled cavity in the
729 polythermal glacier of Tête Rousse, *GEOPHYSICS* **81**, no. 1, WA131–WA146, doi:
730 10.1190/geo2015-0125.1.
731 Garcia, L., K. Luttrell, D. Kilb, and F. Walter (2019). Joint geodetic and seismic analysis of
732 surface crevassing near a seasonal glacier-dammed lake at Gornergletscher, Switzerland,
733 *Annals of Glaciology*, 1–13, doi: 10.1017/aog.2018.32.
734 Gibbons, S. J., and F. Ringdal (2006). The detection of low magnitude seismic events using
735 array-based waveform correlation, *Geophysical Journal International* **165**, no. 1, 149–166,
736 doi: 10.1111/j.1365-246X.2006.02865.x.
737 Gilbert, A., A. Sinisalo, T. R. Gurung, K. Fujita, S. B. Maharjan, T. C. Sherpa, and T. Fukuda
738 (2020). The influence of water percolation through crevasses on the thermal regime of a
739 Himalayan mountain glacier, *The Cryosphere* **14**, no. 4, 1273–1288, doi:
740 https://doi.org/10.5194/tc-14-1273-2020.
741 Gimbert, F., V. C. Tsai, J. M. Amundson, T. C. Bartholomaus, and J. I. Walter (2016).
742 Subseasonal changes observed in subglacial channel pressure, size, and sediment transport,
743 *Geophys*. *Res*. *Lett*. **43**, no. 8, 2016GL068337, doi: 10.1002/2016GL068337.
744 Gimbert, F., V. C. Tsai, and M. P. Lamb (2014). A physical model for seismic noise generation
745 by turbulent flow in rivers, *J*. *Geophys*. *Res*. *Earth Surf*. **119**, no. 10, 2209–2238, doi:
746 10.1002/2014JF003201.
747 Hansen, P. C., and D. P. O'Leary (1993). The Use of the L-Curve in the Regularization of
748 Discrete Ill-Posed Problems, *SIAM J*. *Sci*. *Comput*. **14**, no. 6, 1487–1503, doi:
749 10.1137/0914086.
750 Hantz, D., and L. Lliboutry (1983). Waterways, Ice Permeability at Depth, and Water Pressures
751 at Glacier D'Argentière, French Alps, *Journal of Glaciology* **29**, no. 102, 227–239, doi:
752 10.3189/S0022143000008285.
753 Helmstetter, A., L. Moreau, B. Nicolas, P. Comon, and M. Gay (2015). Intermediate-depth
754 icequakes and harmonic tremor in an Alpine glacier (Glacier d'Argentière, France): Evidence
755 for hydraulic fracturing?, *J*. *Geophys*. *Res*. *Earth Surf*. **120**, no. 3, 2014JF003289, doi:
756 10.1002/2014JF003289.
757 Helmstetter, A., B. Nicolas, P. Comon, and M. Gay (2015). Basal icequakes recorded beneath
758 an Alpine glacier (Glacier d'Argentière, Mont Blanc, France): Evidence for stick-slip

759 motion?, *J. Geophys. Res. Earth Surf.* **120**, no. 3, 2014JF003288, doi:
760 10.1002/2014JF003288.
761 Herring, T. A., R. W. King, M. A. Floyd, and S. C. McClusky (2018). Introduction to
762 GAMIT/GLOBK, *Department of Earth, Atmospheric and Planetary Sciences, Massachussetts*
763 *Institute of Technology*, 54.
764 Herrmann, R. B. (2013). Computer Programs in Seismology: An Evolving Tool for Instruction
765 and Research, *Seismological Research Letters* **84**, no. 6, 1081–1088, doi:
766 10.1785/0220110096.
767 Iken, A. (1981). The Effect of the Subglacial Water Pressure on the Sliding Velocity of a
768 Glacier in an Idealized Numerical Model, *Journal of Glaciology* **27**, no. 97, 407–421, doi:
769 10.3189/S0022143000011448.
770 Iken, A., and R. A. Bindschadler (1986). Combined measurements of Subglacial Water
771 Pressure and Surface Velocity of Findelengletscher, Switzerland: Conclusions about Drainage
772 System and Sliding Mechanism, *Journal of Glaciology* **32**, no. 110, 101–119, doi:
773 10.3189/S0022143000006936.
774 Iken, A., K. Echelmeyer, W. Harrison, and M. Funk (1993). Mechanisms of fast flow in
775 Jakobshavns Isbræ, West Greenland: Part I. Measurements of temperature and water level in
776 deep boreholes, *Journal of Glaciology* **39**, no. 131, 15–25, doi: 10.3189/S0022143000015689.
777 Inbal, A., J. P. Ampuero, and R. W. Clayton (2016). Localized seismic deformation in the upper
778 mantle revealed by dense seismic arrays, *Science* **354**, no. 6308, 88–92, doi:
779 10.1126/science.aaf1370.
780 Kraaijenbrink, P. D. A., J. M. Shea, F. Pellicciotti, S. M. de Jong, and W. W. Immerzeel (2016).
781 Object-based analysis of unmanned aerial vehicle imagery to map and characterise surface
782 features on a debris-covered glacier, *Remote Sensing of Environment* **186**, 581–595, doi:
783 10.1016/j.rse.2016.09.013.
784 Krug, J., J. Weiss, O. Gagliardini, and G. Durand (2014). Combining damage and fracture
785 mechanics to model calving, *The Cryosphere* **8**, no. 6, 2101–2117, doi: 10.5194/tc-8-2101-
786 2014.
787 Lagarias, J., J. Reeds, M. Wright, and P. Wright (1998). Convergence Properties of the Nelder--
788 Mead Simplex Method in Low Dimensions, *SIAM Journal on Optimization* **9**, 112–147, doi:
789 10.1137/S1052623496303470.
790 Li, Z., Z. Peng, D. Hollis, L. Zhu, and J. McClellan (2018). High-resolution seismic event
791 detection using local similarity for Large-N arrays, 1, *Sci Rep* **8**, no. 1, 1–10, doi:
792 10.1038/s41598-018-19728-w.
793 Lin, F.-C., D. Li, R. W. Clayton, and D. Hollis (2013). High-resolution 3D shallow crustal
794 structure in Long Beach, California: Application of ambient noise tomography on a dense
795 seismic array, *Geophysics* **78**, no. 4, Q45–Q56, doi: 10.1190/geo2012-0453.1.
796 Lindner, F., G. Laske, F. Walter, and A. K. Doran (2019). Crevasse-induced Rayleigh-wave
797 azimuthal anisotropy on Glacier de la Plaine Morte, Switzerland, *Annals of Glaciology*, 1–16,
798 doi: 10.1017/aog.2018.25.
799 Lindner, F., F. Walter, G. Laske, and F. Gimbert (2020). Glaciohydraulic seismic tremors on an
800 Alpine glacier, *The Cryosphere* **14**, no. 1, 287–308, doi: https://doi.org/10.5194/tc-14-287-
801 2020.
802 Lipovsky, B. P. (2018). Ice Shelf Rift Propagation and the Mechanics of Wave-Induced
803 Fracture, *Journal of Geophysical Research: Oceans* **123**, no. 6, 4014–4033, doi:
804 10.1029/2017JC013664.
805 Lipovsky, B. P., and E. M. Dunham (2016). Tremor during ice-stream stick slip, *The*
806 *Cryosphere* **10**, no. 1, 385–399, doi: 10.5194/tc-10-385-2016.
807 Lipovsky, B. P., C. R. Meyer, L. K. Zoet, C. McCarthy, D. D. Hansen, A. W. Rempel, and F.
808 Gimbert (2019). Glacier sliding, seismicity and sediment entrainment, *Annals of Glaciology*,

809 1–11, doi: 10.1017/aog.2019.24.
810 Lliboutry, L. (1968). General theory of subglacial cavitation and sliding of temperate glaciers,
811 *Journal of Glaciology* **7**, 21–58.
812 Lliboutry, L. (1959). Une théorie du frottement du glacier sur son lit, *Annales de Geophysique*
813 **15**, 250.
814 Lobkis, O. I., and R. L. Weaver (2001). On the emergence of the Green's function in the
815 correlations of a diffuse field, *The Journal of the Acoustical Society of America* **110**, no. 6,
816 3011–3017, doi: 10.1121/1.1417528.
817 Lomax, A., J. Virieux, P. Volant, and C. Berge-Thierry (2000). Probabilistic Earthquake
818 Location in 3D and Layered Models, in *Advances in Seismic Event Location* C. H. Thurber,
819 and N. Rabinowitz(Editors), Springer Netherlands, Dordrecht, Modern Approaches in
820 Geophysics, 101–134, doi: 10.1007/978-94-015-9536-0_5.
821 Mair, D., P. Nienow, M. Sharp, T. Wohlleben, and I. Willis (2002). Influence of subglacial
822 drainage system evolution on glacier surface motion: Haut Glacier d'Arolla, Switzerland, *J*.
823 *Geophys*. *Res*. **107**, no. B8, EPM 8-1, doi: 10.1029/2001JB000514.
824 Meng, H., and Y. Ben-Zion (2018). Detection of small earthquakes with dense array data:
825 example from the San Jacinto fault zone, southern California, *Geophys J Int* **212**, no. 1, 442–
826 457, doi: 10.1093/gji/ggx404.
827 Mikesell, T. D., K. van Wijk, M. M. Haney, J. H. Bradford, H. P. Marshall, and J. T. Harper
828 (2012). Monitoring glacier surface seismicity in time and space using Rayleigh waves,
829 *Journal of Geophysical Research: Earth Surface* **117**, no. F2, doi: 10.1029/2011JF002259.
830 Mingo, L., and G. E. Flowers (2010). An integrated lightweight ice-penetrating radar system,
831 *Journal of Glaciology* **56**, no. 198, 709–714, doi: 10.3189/002214310793146179.
832 Mordret, A., M. Landès, N. M. Shapiro, S. C. Singh, P. Roux, and O. I. Barkved (2013). Near-
833 surface study at the Valhall oil field from ambient noise surface wave tomography, *Geophys J*
834 *Int* **193**, no. 3, 1627–1643, doi: 10.1093/gji/ggt061.
835 Moreau, L. (1999). Explications et synthèse des variations de l'hydrographie sous-glaciaire du
836 glacier d'Argentière, Mont-Blanc, grâce aux mesures de l'écoulement du glacier sur son lit
837 rocheux de 1970 à 1998, *La Houille Blanche*, no. 5, 40–46, doi: 10.1051/lhb/1999056.
838 Nanni, U., F. Gimbert, C. Vincent, D. Gräff, F. Walter, L. Piard, and L. Moreau (2020).
839 Quantification of seasonal and diurnal dynamics of subglacial channels using seismic
840 observations on an Alpine glacier, *The Cryosphere* **14**, no. 5, 1475–1496, doi:
841 https://doi.org/10.5194/tc-14-1475-2020.
842 Neave, K. G., and J. C. Savage (1970). Icequakes on the Athabasca Glacier, *Journal of*
843 *Geophysical Research (1896-1977)* **75**, no. 8, 1351–1362, doi: 10.1029/JB075i008p01351.
844 Nelder, J. A., and R. Mead (1965). A Simplex Method for Function Minimization, *The*
845 *Computer Journal* **7**, no. 4, 308–313, doi: 10.1093/comjnl/7.4.308.
846 Podolskiy, E. A., K. Fujita, S. Sunako, A. Tsushima, and R. B. Kayastha (2018). Nocturnal
847 Thermal Fracturing of a Himalayan Debris-Covered Glacier Revealed by Ambient Seismic
848 Noise, *Geophysical Research Letters* **45**, no. 18, 9699–9709, doi: 10.1029/2018GL079653.
849 Podolskiy, E. A., and F. Walter (2016). Cryoseismology, *Rev*. *Geophys*. **54**, no. 4,
850 2016RG000526, doi: 10.1002/2016RG000526.
851 Preiswerk, L. E., C. Michel, F. Walter, and D. Fäh (2019). Effects of geometry on the seismic
852 wavefield of Alpine glaciers, *Annals of Glaciology* **60**, no. 79, 112–124, doi:
853 10.1017/aog.2018.27.
854 Ringler, A. T., R. E. Anthony, M. S. Karplus, A. A. Holland, and D. C. Wilson (2018).
855 Laboratory Tests of Three Z-Land Fairfield Nodal 5-Hz, Three-Component Sensors,
856 *Seismological Research Letters* **89**, no. 5, 1601–1608, doi: 10.1785/0220170236.
857 Ritz, C., T. L. Edwards, G. Durand, A. J. Payne, V. Peyaud, and R. C. A. Hindmarsh (2015).
858 Potential sea-level rise from Antarctic ice-sheet instability constrained by observations,

859 *Nature* **528**, no. 7580, 115–118, doi: 10.1038/nature16147.
860 Roeoesli, C., F. Walter, J.-P. Ampuero, and E. Kissling (2016). Seismic moulin tremor, *J*.
861 *Geophys*. *Res*. *Solid Earth* **121**, no. 8, 2015JB012786, doi: 10.1002/2015JB012786.
862 Rost, S., and C. Thomas (2002). Array Seismology: Methods and Applications, *Reviews of*
863 *Geophysics* **40**, no. 3, 2-1-2–27, doi: 10.1029/2000RG000100.
864 Roux, P.-F., D. Marsan, J.-P. Métaxian, G. O'Brien, and L. Moreau (2008). Microseismic
865 activity within a serac zone in an alpine glacier (Glacier d'Argentière, Mont Blanc, France),
866 *Journal of Glaciology* **54**, no. 184, 157–168, doi: 10.3189/002214308784409053.
867 Roux, P., L. Moreau, A. Lecointre, G. Hillers, M. Campillo, Y. Ben-Zion, D. Zigone, and F.
868 Vernon (2016). A methodological approach towards high-resolution surface wave imaging of
869 the San Jacinto Fault Zone using ambient-noise recordings at a spatially dense array, *Geophys*
870 *J Int* **206**, no. 2, 980–992, doi: 10.1093/gji/ggw193.
871 Roux, P.-F., F. Walter, P. Riesen, S. Sugiyama, and M. Funk (2010). Observation of surface
872 seismic activity changes of an Alpine glacier during a glacier-dammed lake outburst, *Journal*
873 *of Geophysical Research: Earth Surface* **115**, no. F3, doi: 10.1029/2009JF001535.
874 Roux, P., M. Wathelet, and A. Roueff (2011). The San Andreas Fault revisited through seismic-
875 noise and surface-wave tomography, *Geophysical Research Letters* **38**, no. 13, doi:
876 10.1029/2011GL047811.
877 Scherler, D., B. Bookhagen, and M. R. Strecker (2011). Spatially variable response of
878 Himalayan glaciers to climate change affected by debris cover, 3, *Nature Geoscience* **4**, no. 3,
879 156–159, doi: 10.1038/ngeo1068.
880 Schoof, C. (2010). Ice-sheet acceleration driven by melt supply variability, *Nature* **468**, no.
881 7325, 803–806, doi: 10.1038/nature09618.
882 Schoof, C. (2005). The effect of cavitation on glacier sliding, *Proceedings of the Royal Society*
883 *of London A: Mathematical, Physical and Engineering Sciences* **461**, no. 2055, 609–627, doi:
884 10.1098/rspa.2004.1350.
885 Sergeant, A., M. Chmiel, F. Lindner, F. Walter, P. Roux, J. Chaput, F. Gimbert, and A. Mordret
886 (2020). On the Green's function emergence from interferometry of seismic wave fields
887 generated in high-melt glaciers: implications for passive imaging and monitoring, *The*
888 *Cryosphere* **14**, no. 3, 1139–1171, doi: https://doi.org/10.5194/tc-14-1139-2020.
889 Seydoux, L., N. M. Shapiro, J. de Rosny, F. Brenguier, and M. Landès (2016). Detecting
890 seismic activity with a covariance matrix analysis of data recorded on seismic arrays,
891 *Geophys J Int* **204**, no. 3, 1430–1442, doi: 10.1093/gji/ggv531.
892 Stolt, R. H. (1978). Migration by Fourier transform, *Geophysics* **43**, no. 1, 23–48, doi:
893 10.1190/1.1440826.
894 Tedstone, A. J., P. W. Nienow, N. Gourmelen, A. Dehecq, D. Goldberg, and E. Hanna (2015).
895 Decadal slowdown of a land-terminating sector of the Greenland Ice Sheet despite warming,
896 *Nature* **526**, no. 7575, 692–695, doi: 10.1038/nature15722.
897 Tsai, V. C., B. Minchew, M. P. Lamb, and J.-P. Ampuero (2012). A physical model for seismic
898 noise generation from sediment transport in rivers, *Geophysical Research Letters* **39**, no. 2,
899 L02404, doi: 10.1029/2011GL050255.
900 Tsai, V. C., and J. R. Rice (2010). A model for turbulent hydraulic fracture and application to
901 crack propagation at glacier beds, *Journal of Geophysical Research: Earth Surface* **115**, no.
902 F3, n/a–n/a, doi: 10.1029/2009JF001474.
903 Vallon, M. (1967). Contribution à l'étude de la Mer de Glace - Alpes françaises, phdthesis,
904 Faculté des Sciences de l'Université de Grenoble.
905 Vandemeulebrouck, J., P. Roux, and E. Cros (2013). The plumbing of Old Faithful Geyser
906 revealed by hydrothermal tremor, *Geophysical Research Letters* **40**, no. 10, 1989–1993, doi:
907 10.1002/grl.50422.
908 Veen, C. J. van der (2007). Fracture propagation as means of rapidly transferring surface

meltwater to the base of glaciers, *Geophysical Research Letters* **34**, no. 1, doi: 10.1029/2006GL028385.
van der Veen, C. J. (1998). Fracture mechanics approach to penetration of surface crevasses on glaciers, *Cold Regions Science and Technology* **27**, no. 1, 31–47, doi: 10.1016/S0165-232X(97)00022-0.
Vincent, C., and L. Moreau (2016). Sliding velocity fluctuations and subglacial hydrology over the last two decades on Argentière glacier, Mont Blanc area, *Journal of Glaciology*, 1–11, doi: 10.1017/jog.2016.35.
Vincent, C., A. Soruco, M. F. Azam, R. Basantes-Serrano, M. Jackson, B. Kjøllmoen, E. Thibert, P. Wagnon, D. Six, A. Rabatel, *et al*. (2018). A Nonlinear Statistical Model for Extracting a Climatic Signal From Glacier Mass Balance Measurements, *Journal of Geophysical Research: Earth Surface* **123**, no. 9, 2228–2242, doi: 10.1029/2018JF004702.
Vincent, C., A. Soruco, D. Six, and E. L. Meur (2009). Glacier thickening and decay analysis from 50 years of glaciological observations performed on Glacier d'Argentière, Mont Blanc area, France, *Annals of Glaciology* **50**, no. 50, 73–79, doi: 10.3189/172756409787769500.
Vivian, R., and G. Bocquet (1973). Subglacial Cavitation Phenomena Under the Glacier D'Argentière, Mont Blanc, France, *Journal of Glaciology* **12**, no. 66, 439–451, doi: 10.3189/S0022143000031853.
Waldhauser, F., and W. L. Ellsworth (2000). A Double-Difference Earthquake Location Algorithm: Method and Application to the Northern Hayward Fault, California, *Bulletin of the Seismological Society of America* **90**, no. 6, 1353–1368, doi: 10.1785/0120000006.
Walter, F., J. F. Clinton, N. Deichmann, D. S. Dreger, S. E. Minson, and M. Funk (2009). Moment Tensor Inversions of Icequakes on Gornergletscher, SwitzerlandMoment Tensor Inversions of Icequakes on Gornergletscher, Switzerland, *Bulletin of the Seismological Society of America* **99**, no. 2A, 852–870, doi: 10.1785/0120080110.
Walter, F., D. Gräff, F. Lindner, P. Paitz, M. Köpfli, M. Chmiel, and A. Fichtner (2020). Distributed acoustic sensing of microseismic sources and wave propagation in glaciated terrain, 1, *Nature Communications* **11**, no. 1, 2436, doi: 10.1038/s41467-020-15824-6.
Walter, F., P. Roux, C. Roeoesli, A. Lecointre, D. Kilb, and P.-F. Roux (2015). Using glacier seismicity for phase velocity measurements and Green's function retrieval, *Geophys J Int* **201**, no. 3, 1722–1737, doi: 10.1093/gji/ggv069.
Wathelet, M., J.-L. Chatelain, C. Cornou, G. Di Giulio, B. Guillier, M. Ohrnberger, and A. Savvaidis (2020). Geopsy: A User-Friendly Open-Source Tool Set for Ambient Vibration Processing, *Seismological Research Letters* **91**, doi: 10.1785/0220190360.
Weaver, C. S., and S. D. Malone (1979). Seismic Evidence for Discrete Glacier Motion at the Rock–Ice Interface, *Journal of Glaciology* **23**, no. 89, 171–184, doi: 10.1017/S0022143000029816.
Weiss, J. (2004). Subcritical crack propagation as a mechanism of crevasse formation and iceberg calving, *Journal of Glaciology* **50**, no. 168, 109–115, doi: 10.3189/172756504781830240.
Welch, P. D. (1967). The use of fast Fourier transform for the estimation of power spectra: A method based on time averaging over short, modified periodograms, *IEEE Transactions on audio and electroacoustics* **15**, no. 2, 70–73.
Zhan, Z. (2019). Seismic Noise Interferometry Reveals Transverse Drainage Configuration Beneath the Surging Bering Glacier, *Geophysical Research Letters* **46**, no. 9, 4747–4756, doi: 10.1029/2019GL082411.
Zoet, L. K., B. Carpenter, M. Scuderi, R. B. Alley, S. Anandakrishnan, C. Marone, and M. Jackson (2013). The effects of entrained debris on the basal sliding stability of a glacier, *J. Geophys. Res. Earth Surf.* **118**, no. 2, 656–666, doi: 10.1002/jgrf.20052.
Zwally, H. J., W. Abdalati, T. Herring, K. Larson, J. Saba, and K. Steffen (2002). Surface Melt-

Induced Acceleration of Greenland Ice-Sheet Flow, *Science* **297**, no. 5579, 218–222, doi: 10.1126/science.1072708.

# FIGURES

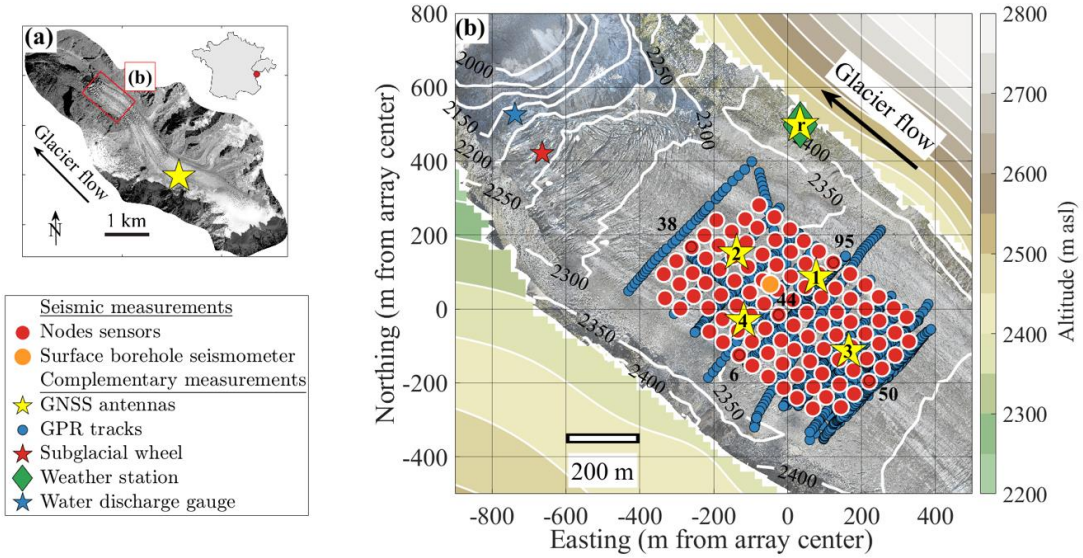


Fig. 1: Maps of the Argentière Glacier and of the instruments deployed during the dense array experiment (see associated legend for symbols correspondence). (a) Aerial picture of the Argentière Glacier taken in 2003. The red rectangle indicates the area shown in Fig. 1(b), which we focus on in this study. The yellow star refers to a permanent GNSS station and the red dot in the inset shows the location of the glacier with respect to French and Swiss borders. (b) Map showing the lower part of the Argentière Glacier along with instrument positions. White contours indicate glacier surface topography as retrieved from structure from motion, and color contours indicate topography outside of the glacier. Symbols refer to instruments as specified in the legend. Numbers associated with red circles indicate nodes that are used for illustrative examples in Fig. 4.

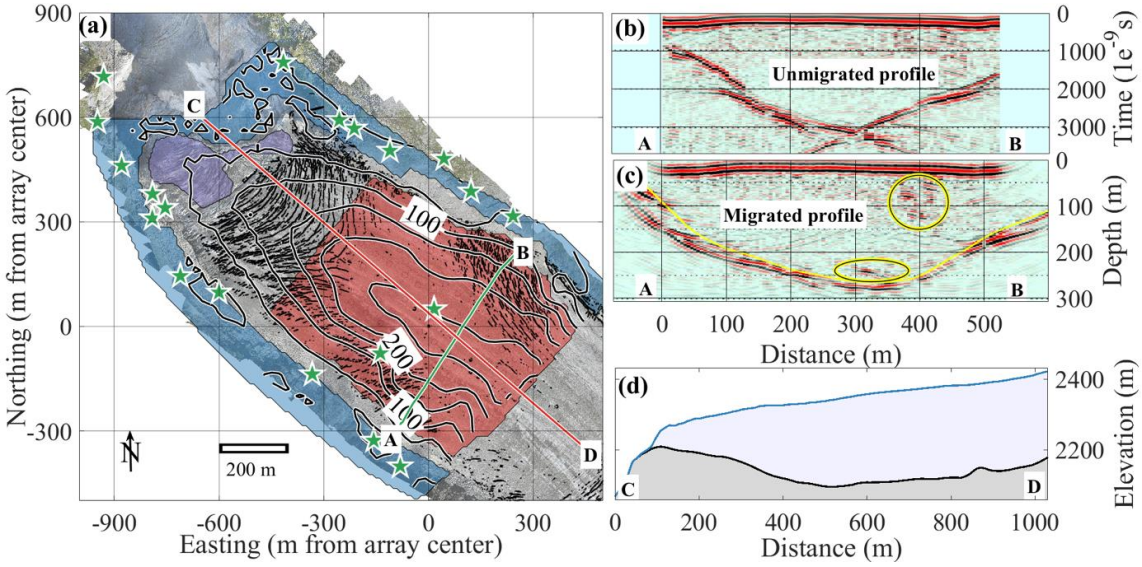


Fig. 2: (a) Ice thickness (black contours) and surface crevasse (black dots) maps. Green stars correspond to the GNSS measured ground control points, while colored areas differentiate between observations used to constrain the bed DEM: the blue area is from a 2018 surface DEM, the purple area corresponds to regions where ice-bed coordinates are known from in-situ

borehole measurements and from excavated tunnels, and the red area corresponds to a region where glacier depth is inferred from the GPR measurements. The green line shows the track associated with the selected GPR profile shown in (b) and (c). The red line shows the profile shown in (d). (b) and (c) Examples of processed (b) unmigrated and (c) migrated GPR data acquired along the AB profile shown in (a). The yellow curve corresponds to the picked interface and the yellow ellipses highlight local reflectivity anomalies. (d) Surface elevation and bed elevation along the CD profile shown in (a).

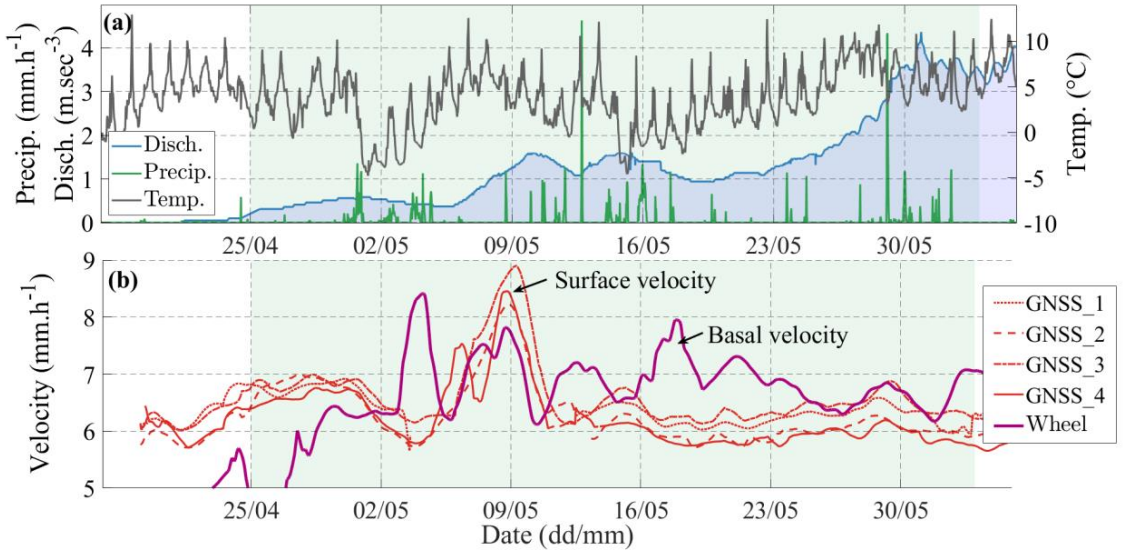


Fig. 3: Time series of meteorological, hydrological and ice dynamic parameters during the dense array experiment (from 25 April to 6 June 2018, shaded in green). (a) Proglacial water discharge (blue), surface temperature (grey) and precipitation (green). (b) Horizontal ice surface measured with GNSS stations (orange lines) and basal sliding measured with at the ice-bed interface (thick purple line). See Nanni *et al*. (2020) for longer time series over the 2016-2018 period.

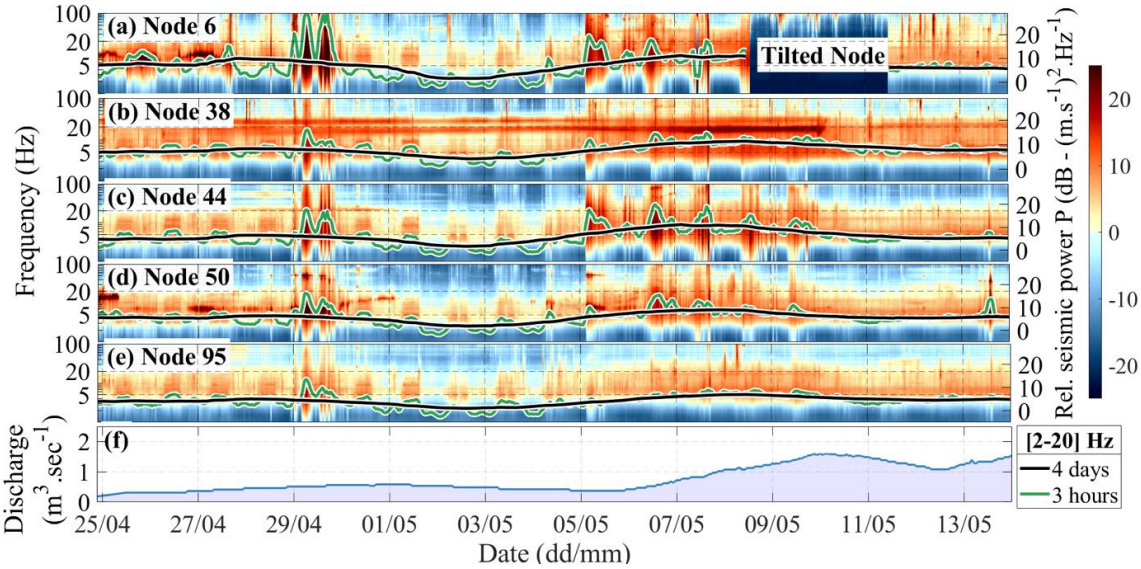

Fig. 4: (a-e) Vertical-component spectrograms calculated at five selected stations across the array (see corresponding numbers in Fig. 1) from 25 April to 5 May 2018. Curves indicate 2-20 Hz frequency-averaged seismic power as smoothed over short (3 hours, green lines) and long (4 days, black lines) periods. See Fig. S1 for spectrograms over the whole period and all stations. (f) Proglacial water discharge timeseries (same as in Fig. 3).

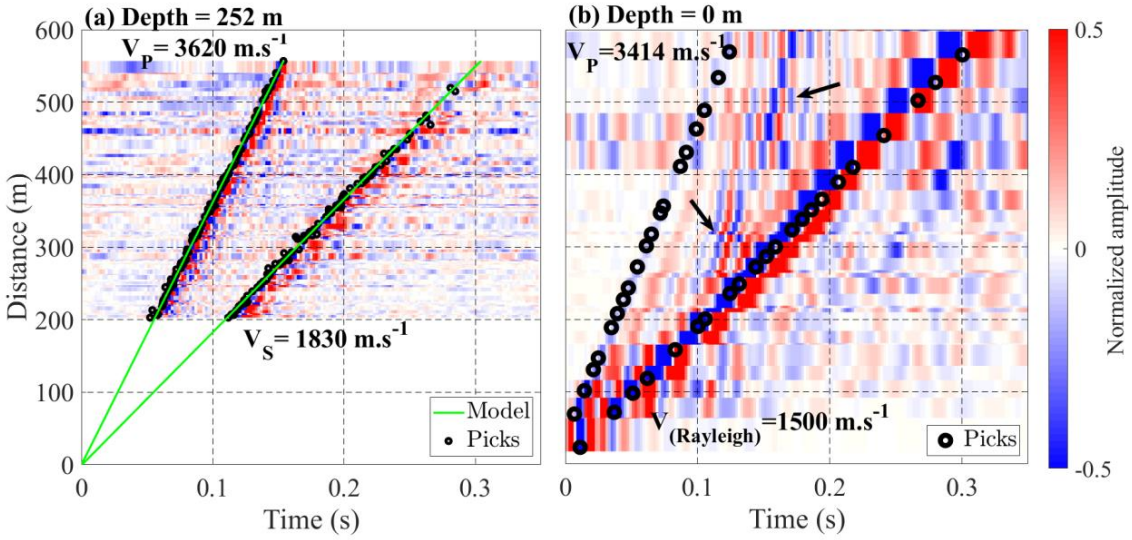


Fig. 5: Vertical-component seismograms of (a) a basal event identified from template matching and (b) a surface event identified from match-field-processing. Corresponding event locations are shown in Fig. 8. Black circles correspond to picked P, S and Rayleigh arrival times and green lines on (a) correspond to predicted arrival times using a P-wave velocity of 3620 m.sec$^{-1}$ and an S-wave velocity of 1830 m.sec$^{-1}$. A hyperbolic arrival is also visible at large offsets on panel b, likely corresponding to a refracted or reflected wave (black arrows). Time origin corresponds to the inferred source time.

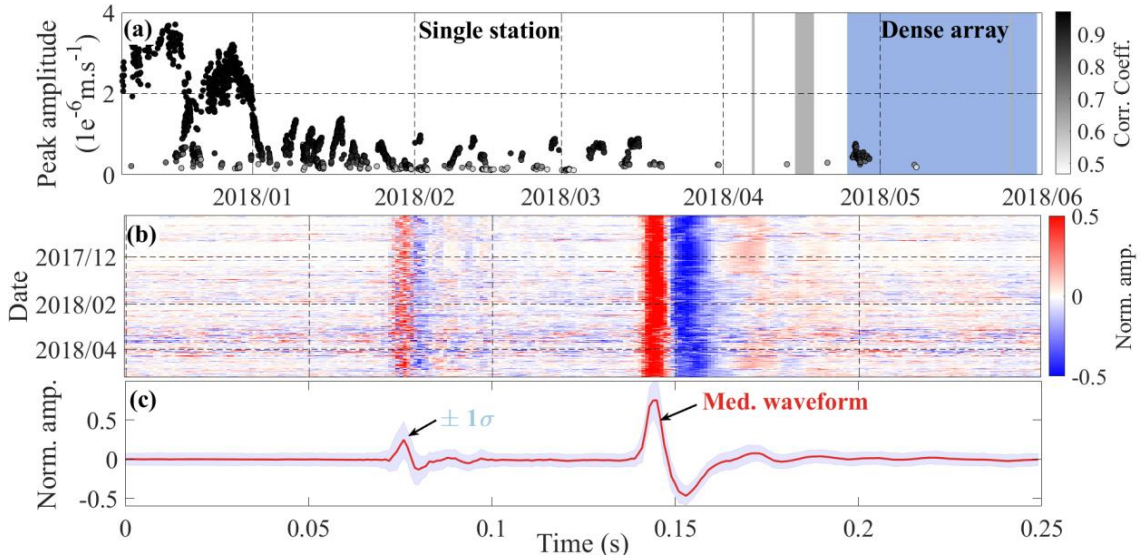


Fig. 6: a) Vertical-component time series of peak amplitude for one cluster of repeating basal events. The grey scale indicates correlation with the template signal. Grey areas indicate gaps in the data and the blue area highlights the time period spanned by our dense-array experiment.

(b) Waveforms of all events of a cluster normalized by peak amplitude (using the North component of the borehole station). The color bar indicates normalized waveform amplitude. Each horizontal line represents one event. Time origin corresponds to the source time. (c) Median seismogram of all events shown in panel (b).

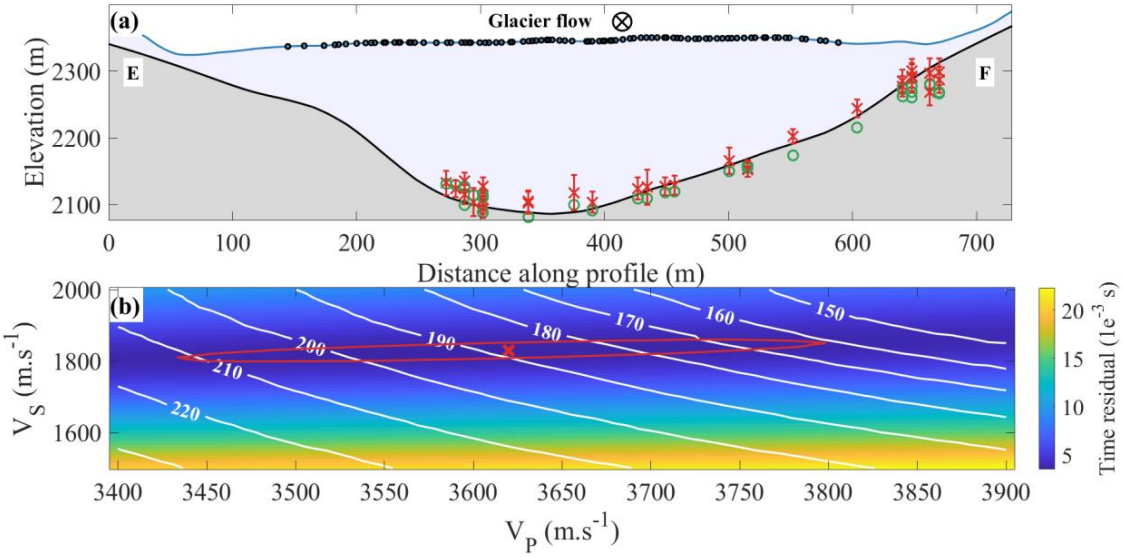


Fig. 7: (a) Two-dimensional representations of stick-slip event locations (red crosses) along the EF profiles shown in Fig. 8. Red error bars show the 95% confidence interval. Green circles indicate the projected depth at the exact location of each event. Black dots show node positions. (b) Average time residuals (background color coded image) and average icequake depth (white contours) as a function of the seismic wave velocities $V_P$ and $V_S$ used to locate basal icequakes. The red cross indicates the velocities $V_P$=3620 m.sec$^{-1}$ and $V_S$=1830 m.sec$^{-1}$ that minimize the average time residuals. The red line delineates the range of $V_P$ and $V_S$ associated with an average residual that is smaller than 105% of the minimum value.

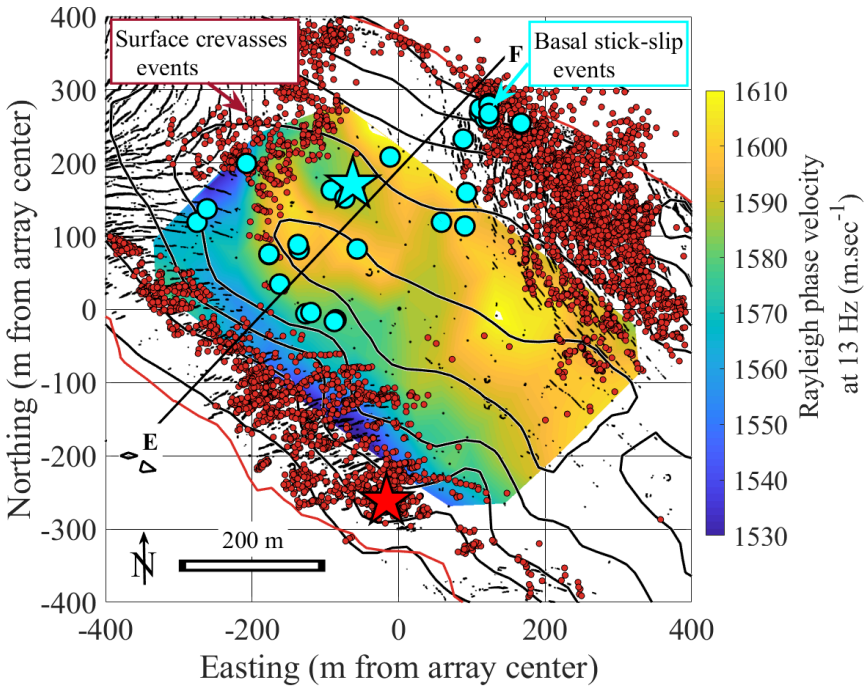


Fig. 8: Map showing the positions of basal stick-slip clusters (filled blue circles) and of icequake events (filled red circles, using signal at 13 Hz and sources with MFP output higher than 0.8). The colored area shows phase velocities from Rayleigh-wave travel-time tomography at 13 Hz. The CD profile refers to the profile used in Fig. 7 and the blue and red stars refer to the events shown in Fig. 5(a) and 5(b), respectively. Black dots show crevasses, contour lines show ice thickness (m) and the red lines delineate the glacier extent.

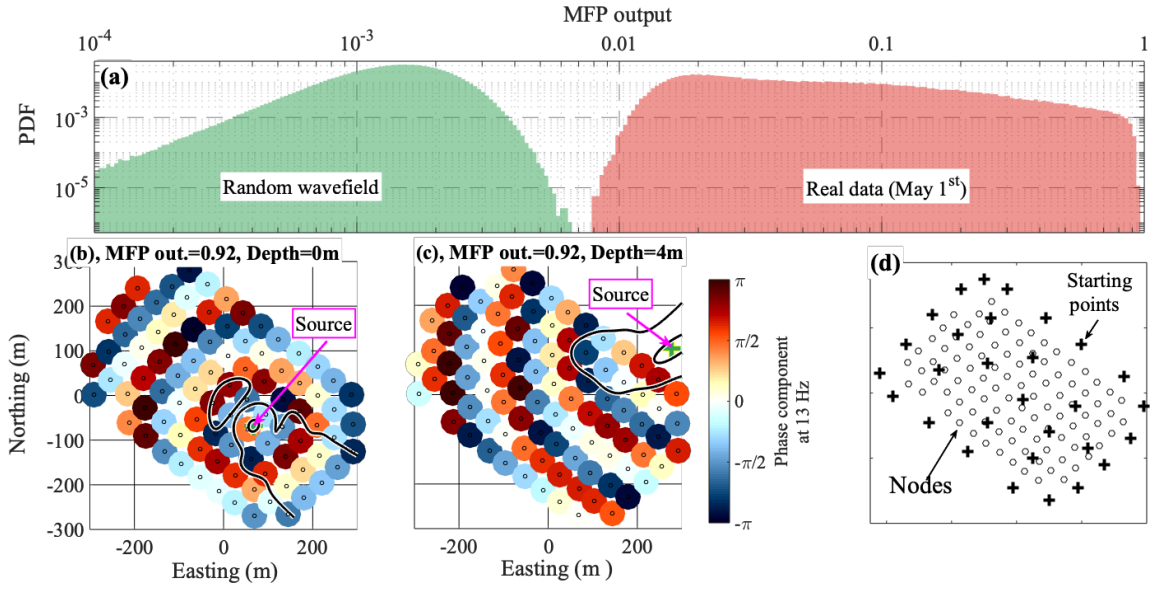


Fig. 9: (a) Probability distribution functions (PDF) of MFP outputs obtained at 13 Hz when applying MFP on one day (1 May 2018) of real data (red) and on a numerically-generated random wavefield (green). The bottom panels (b) and (c) show the phase fields observed over a 1-s time window at 13 Hz for two selected events. Locations obtained from MFP using our minimization process are shown by the pink arrow/green crosses, while the contour lines show 0.1 and 0.8 MFP outputs iso-contours calculated by applying a grid search over the glacier

surface. Panel (d) shows the locations of the 29 starting points (black crosses) used for MFP along with node positions (black circles).

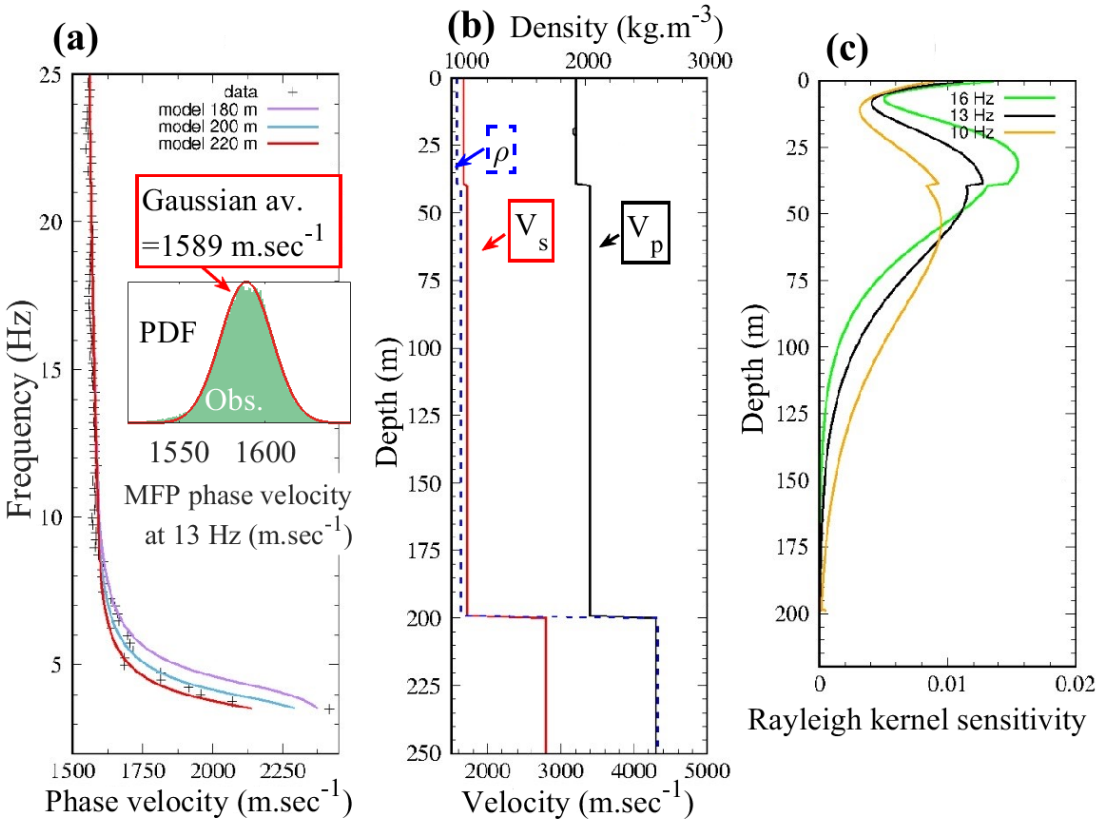


Fig. 10. Inversion of an average one-dimensional structure using an average surface wave dispersion curve. (a) Comparison between the observationally-derived dispersion curve (black crosses) and synthetic Rayleigh wave dispersion curves computed using the elastic model displayed in (b) using glacier thicknesses of 180 m (purple), 200 m (blue) or 220 m (red). The inset shows the distribution of phase velocity obtained from match-field-processing at 13Hz (green) along with a Gaussian fit (red). The central value of the gaussian fit is used to establish the dispersion curve. (b) Synthetic model used to predict the observed dispersion curve. (c) Sensitivity kernels of Rayleigh waves as a function of depth for 16 Hz (green), 13 Hz (black) and 10 Hz (orange) associated with the glacier model shown in (b).

Fig1

Click here to access/download;Figure;fig1_v2.png

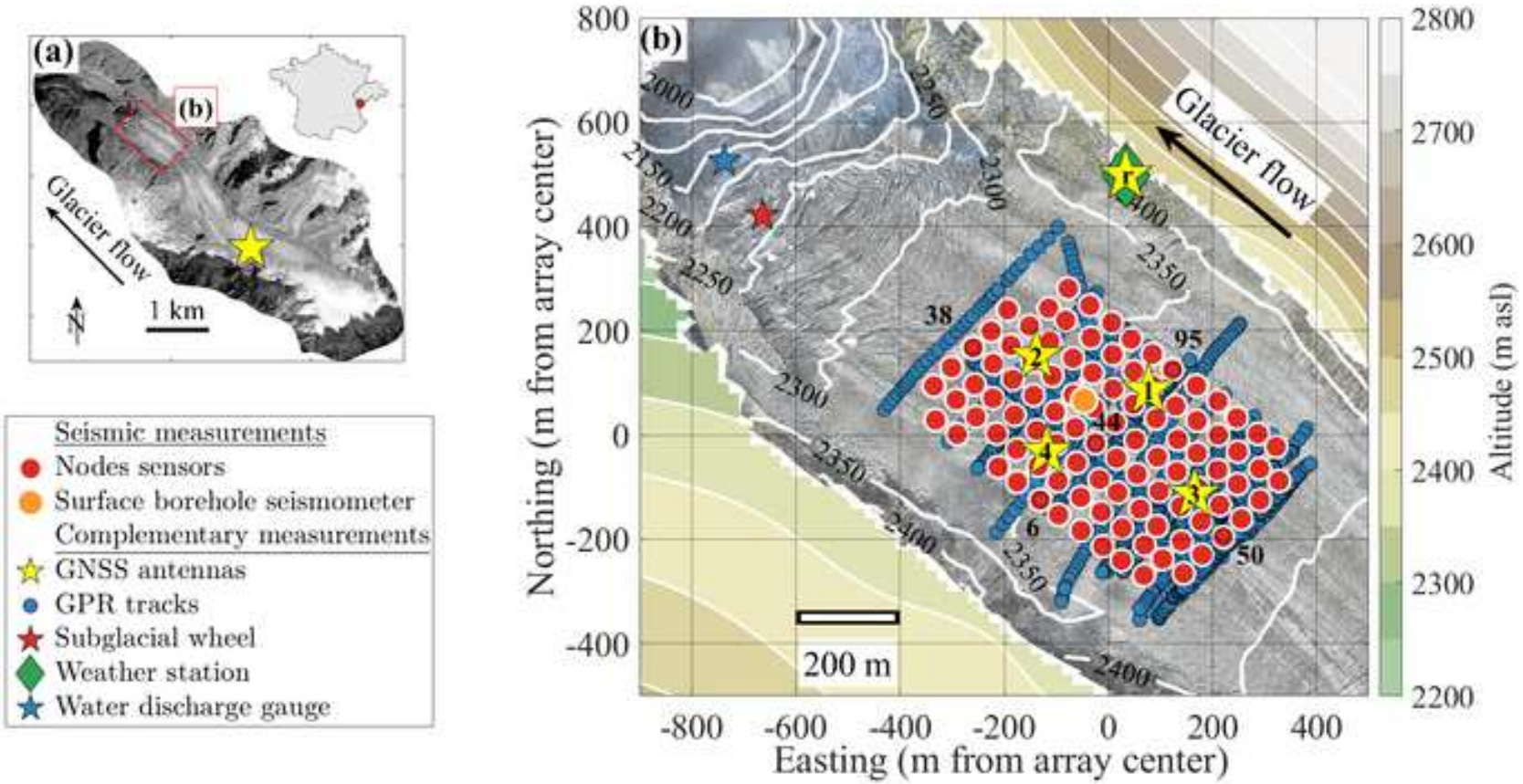

Fig2

Click here to access/download;Figure;fig2_v2.png

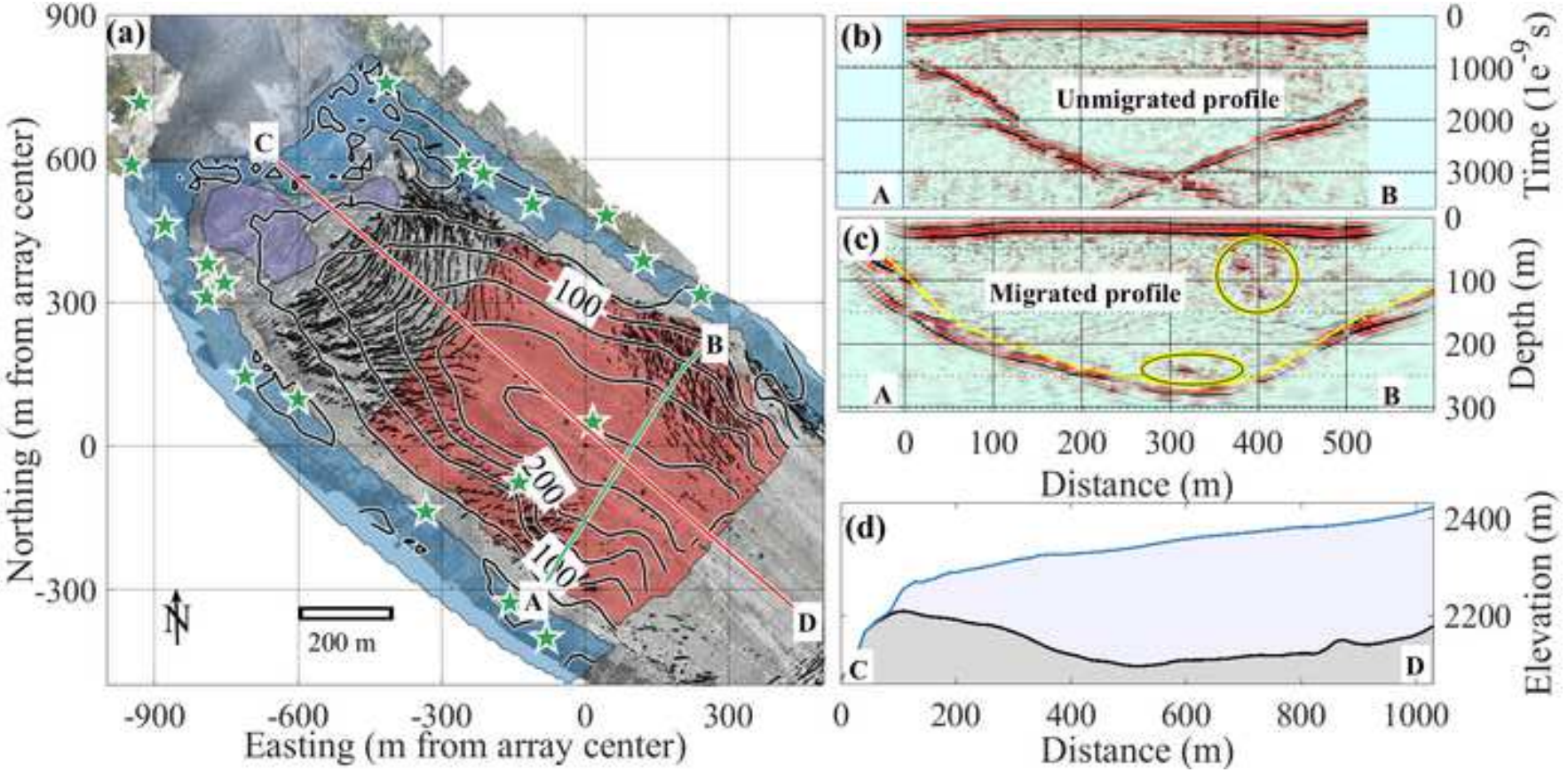

Fig3

Click here to access/download;Figure;fig3_v2.png

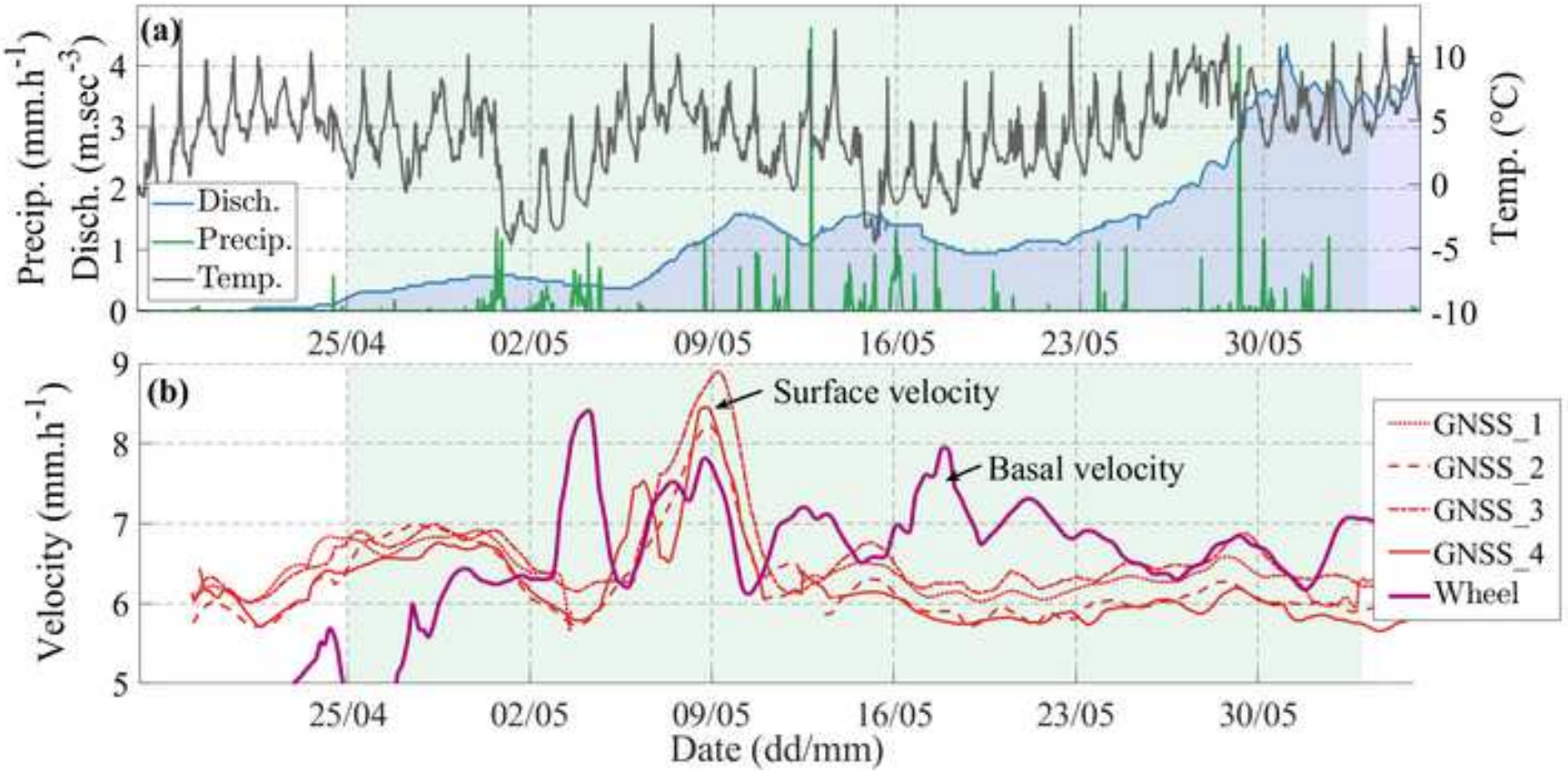

Fig4

Click here to access/download;Figure;fig4_v2.png

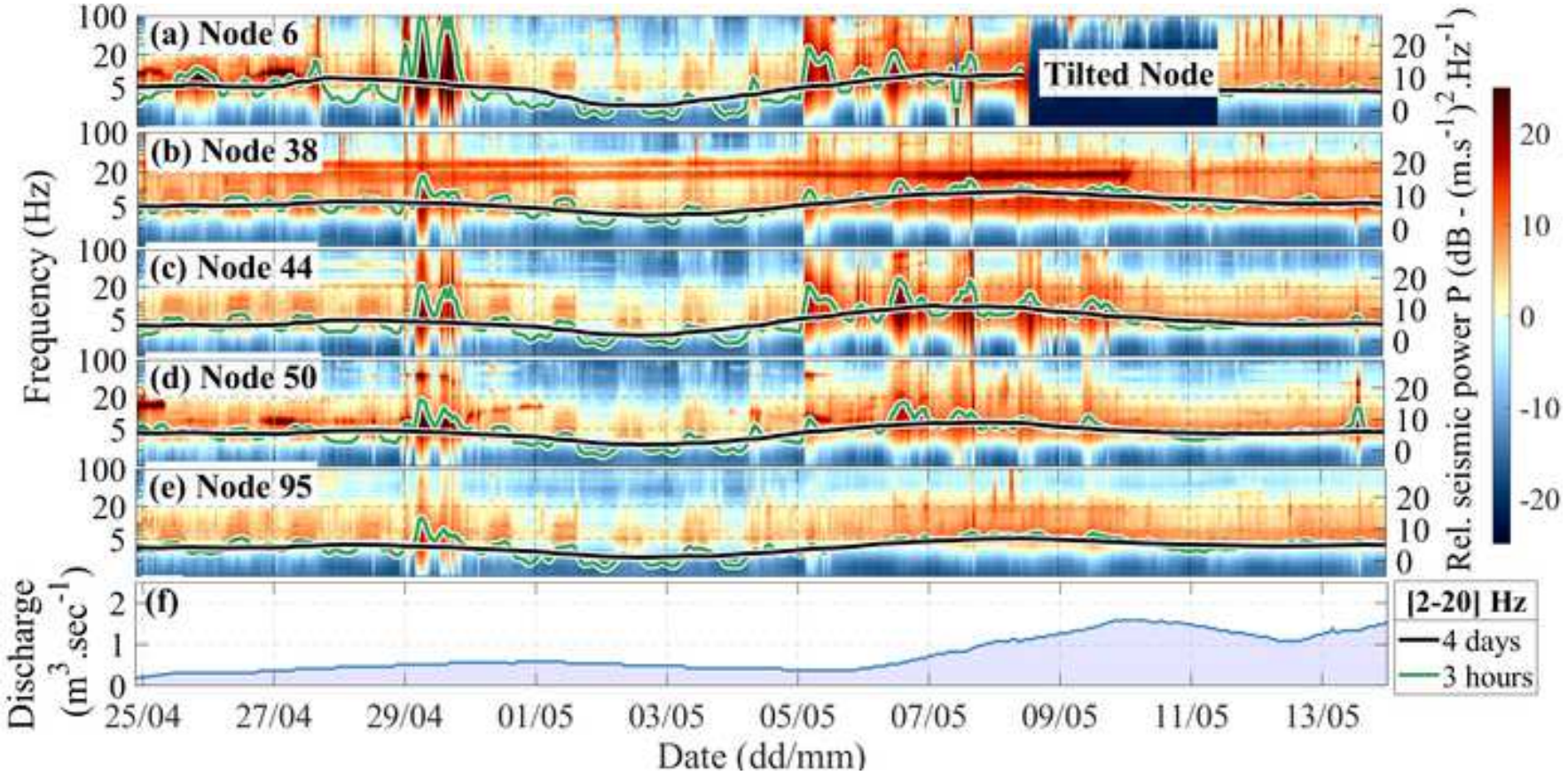

Fig5

Click here to access/download;Figure;fig5.png

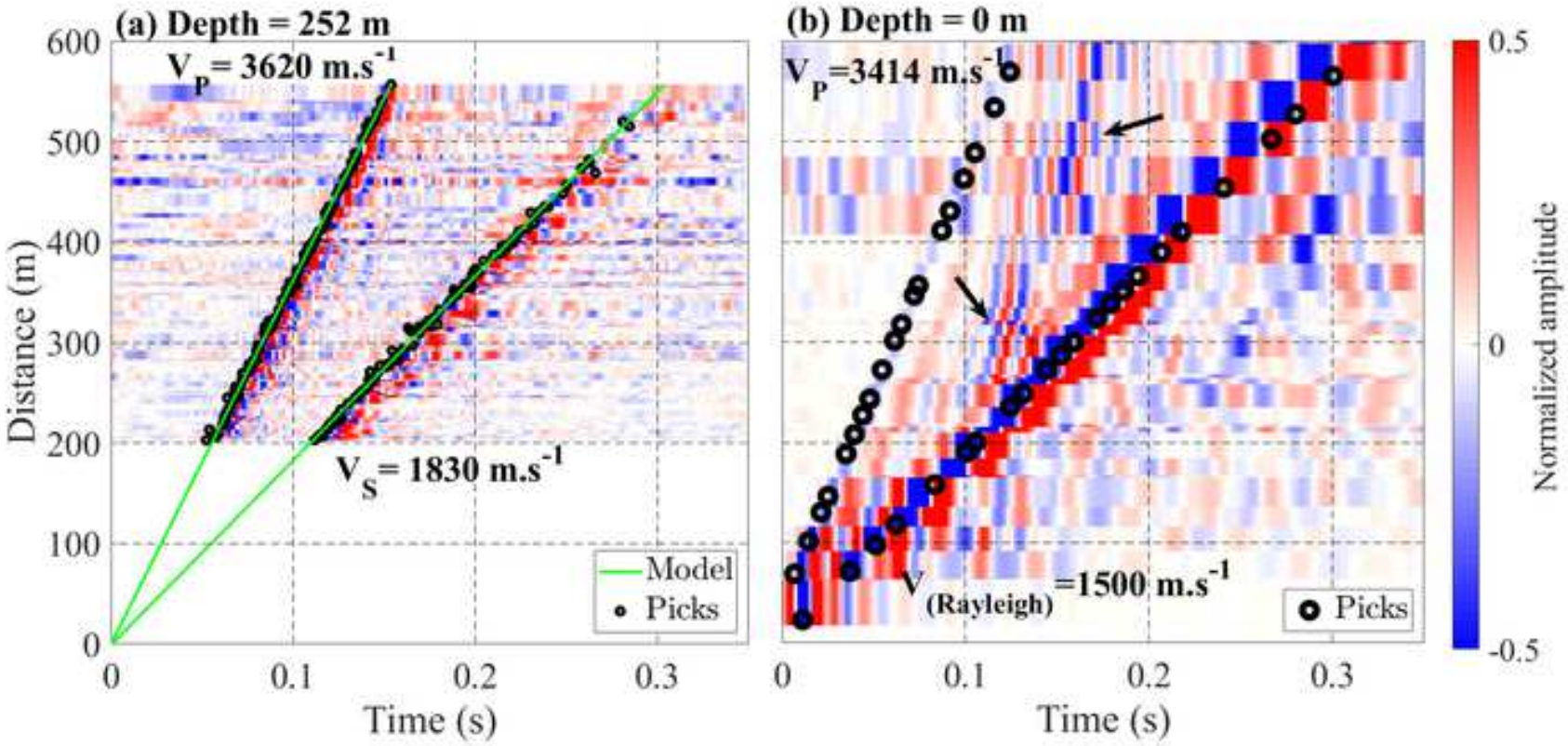

Fig6

Click here to access/download;Figure;fig6_v2.png

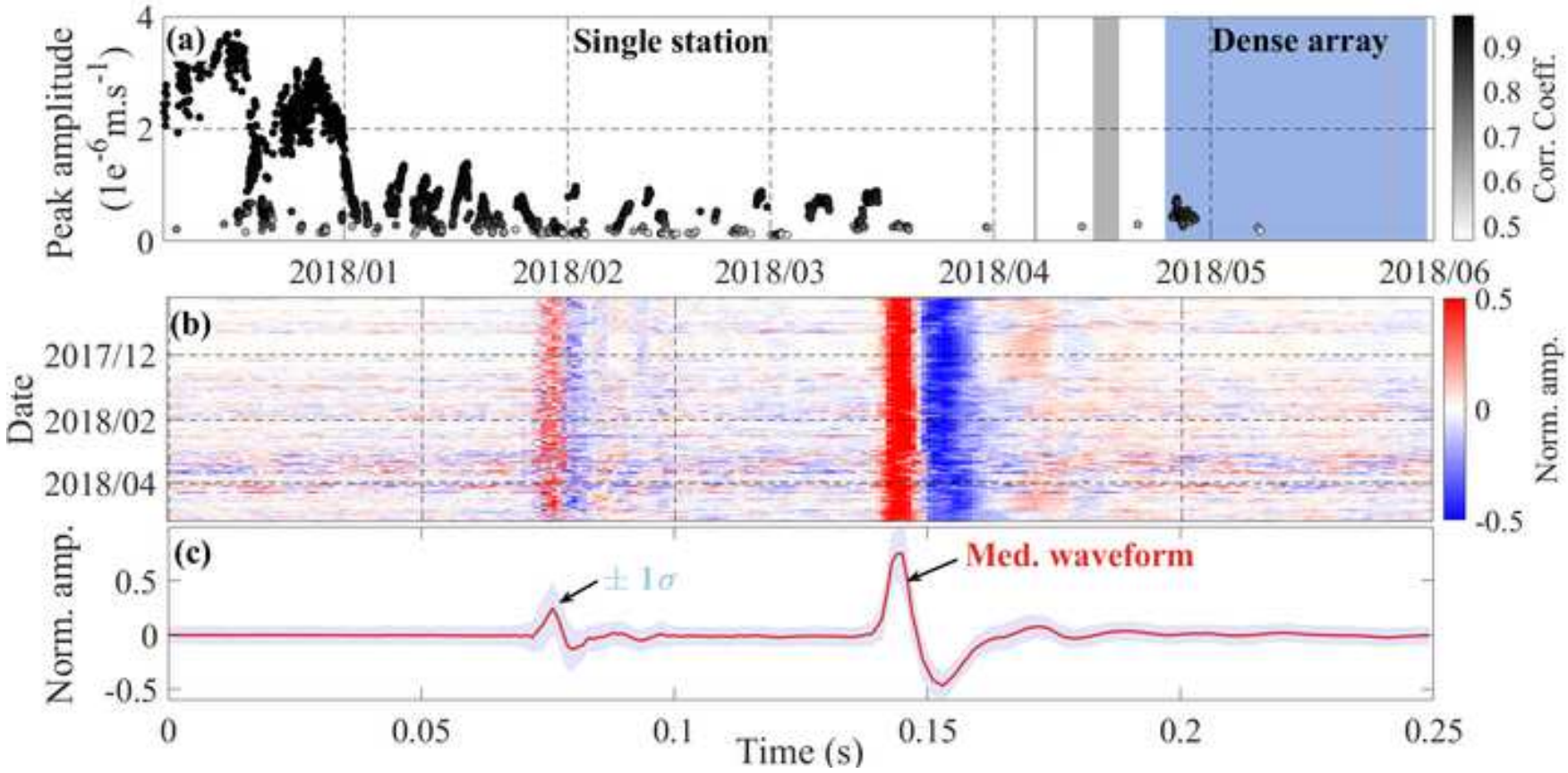

Fig7

Click here to access/download;Figure;fig7_v3.png

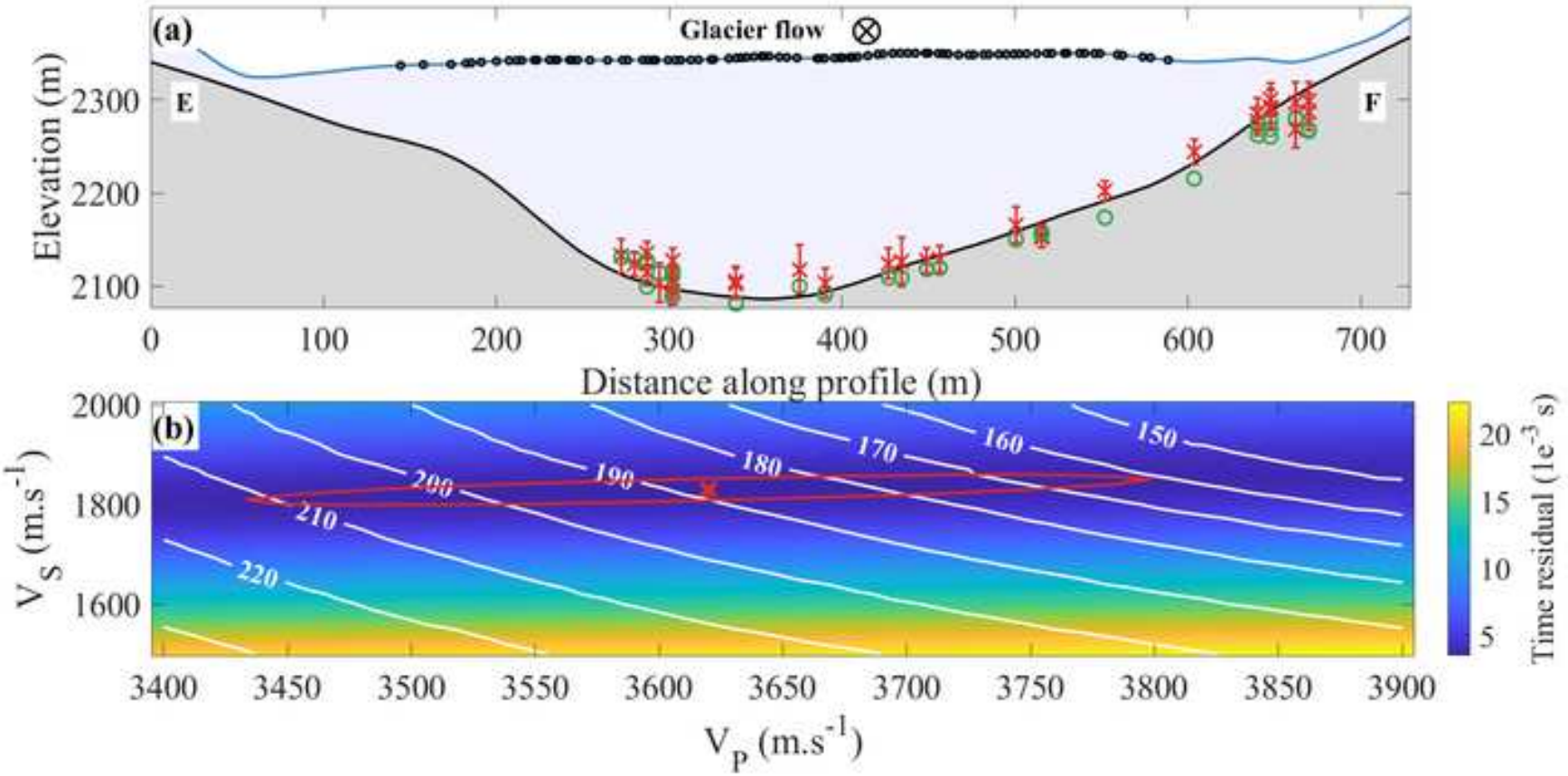

Fig8

Click here to access/download;Figure;fig8_v6.png

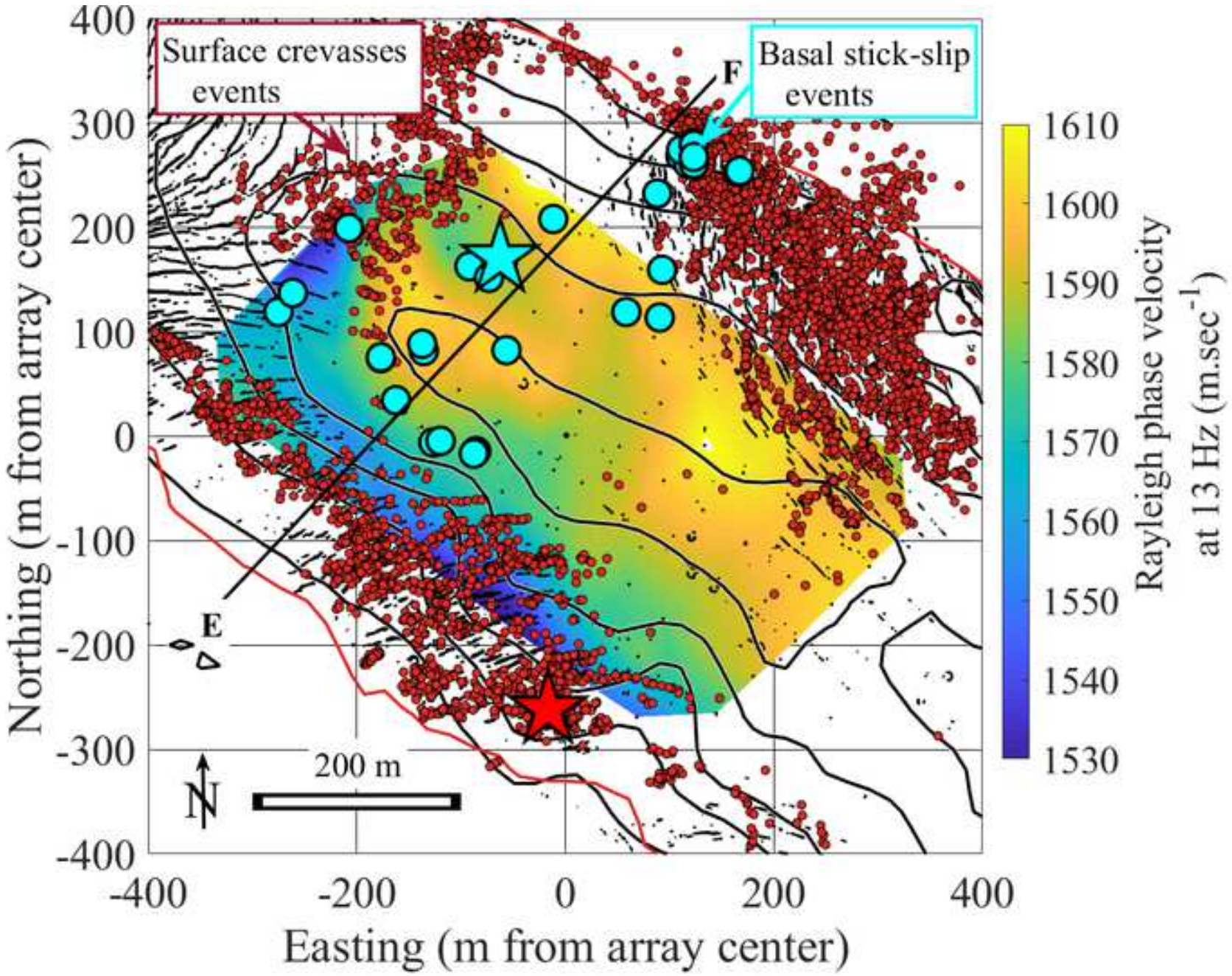

Fig9

Click here to access/download;Figure;fig9.png

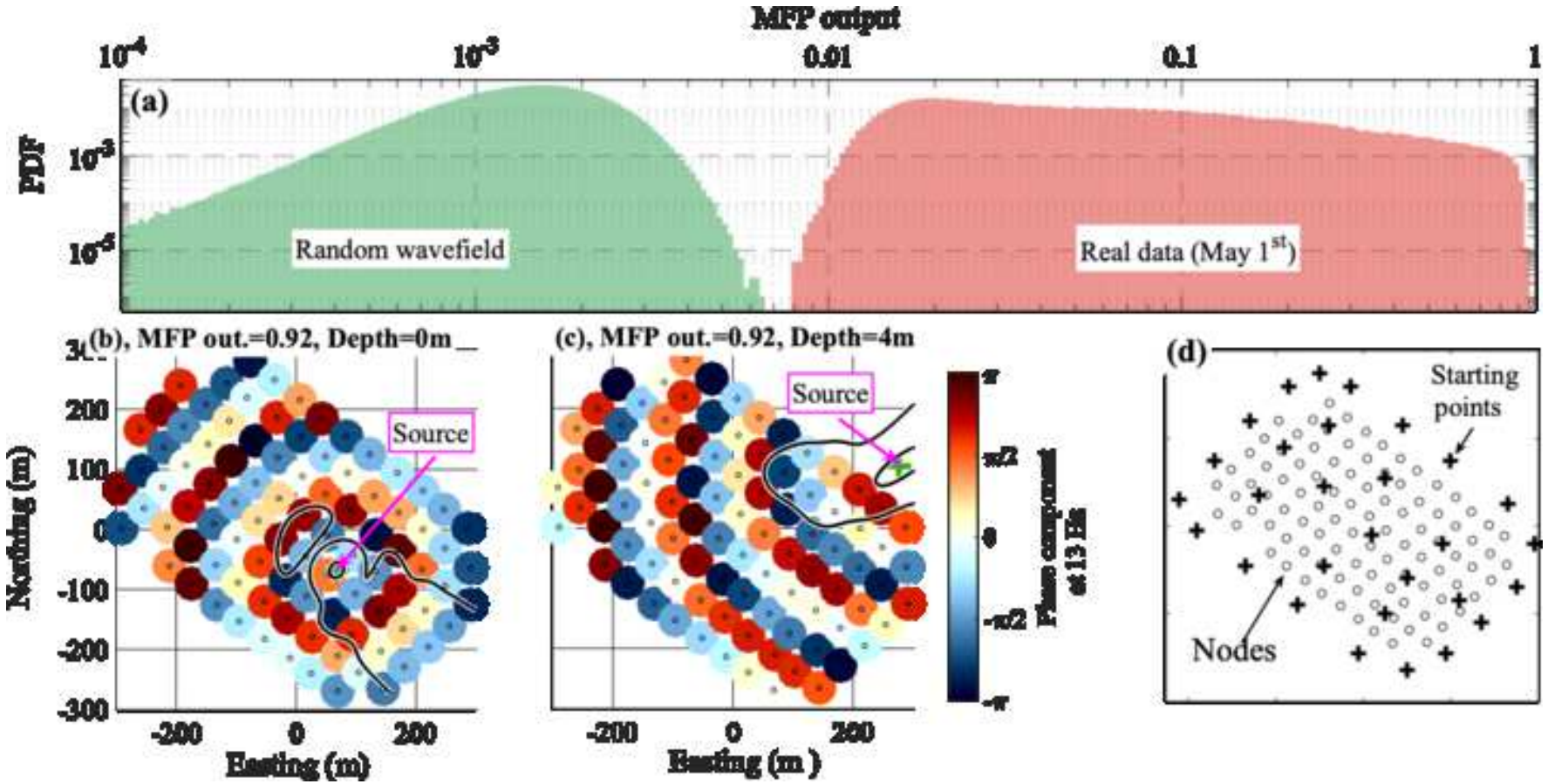

Fig10

Click here to access/download;Figure;fig10.png

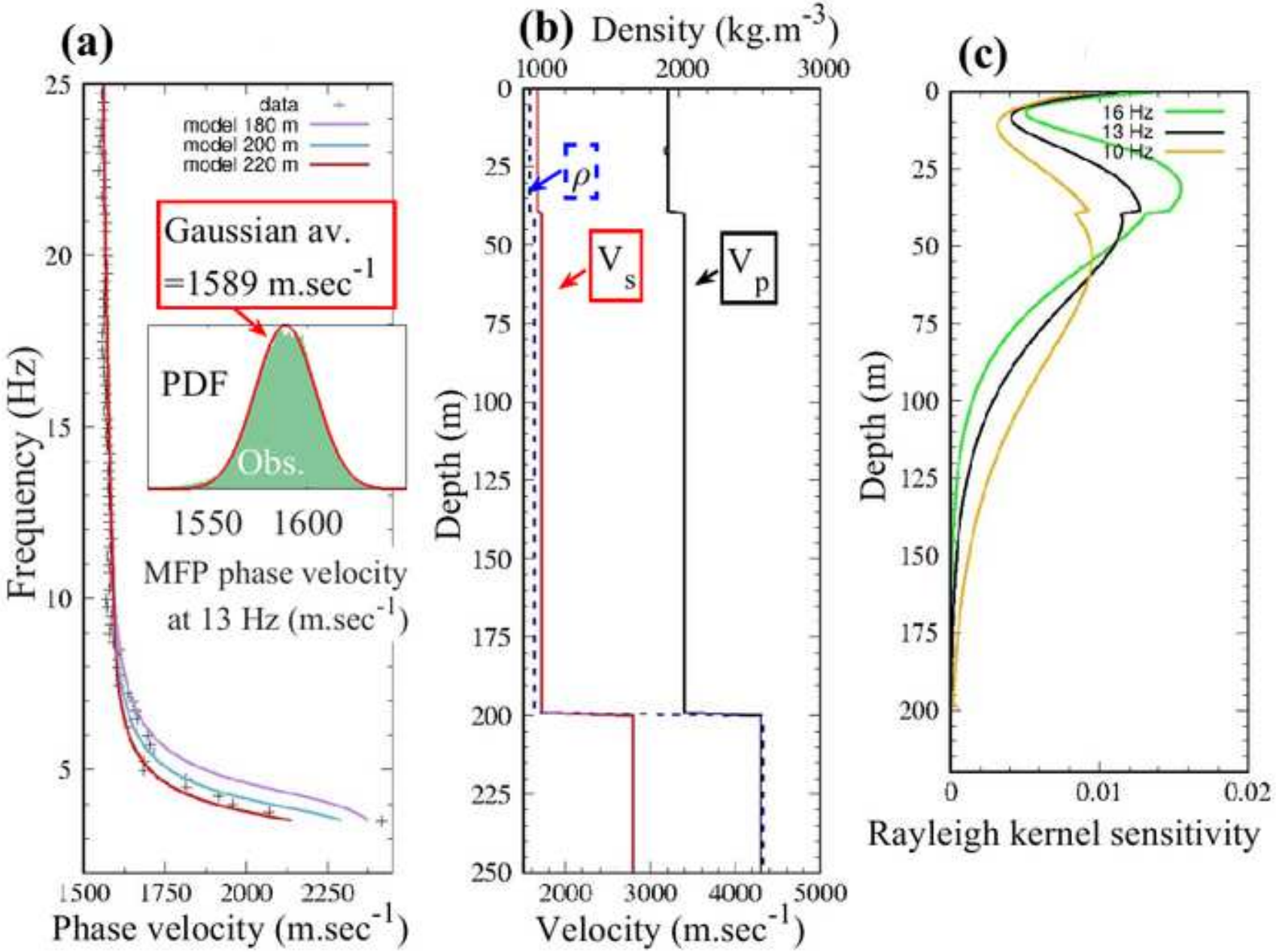

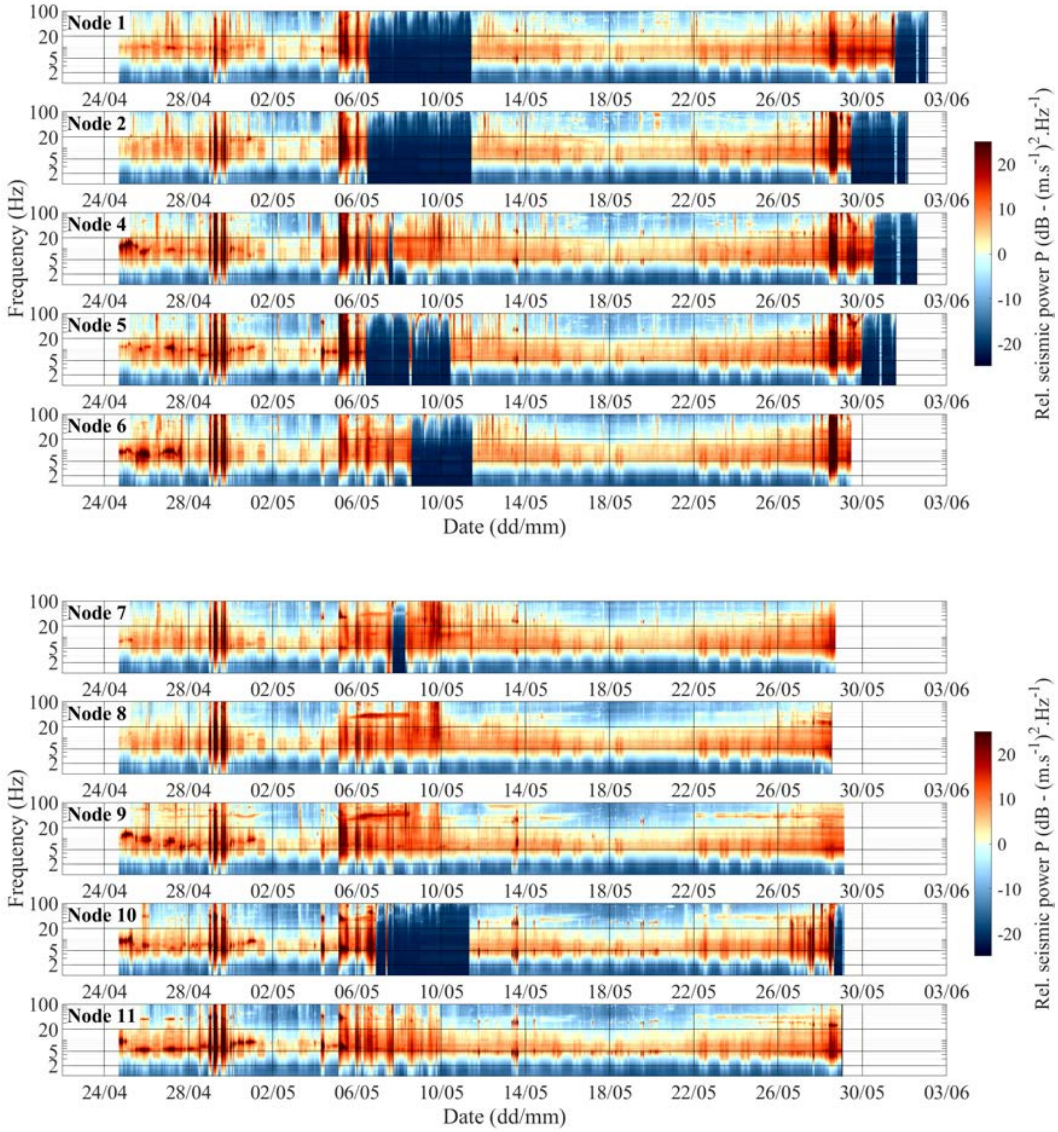

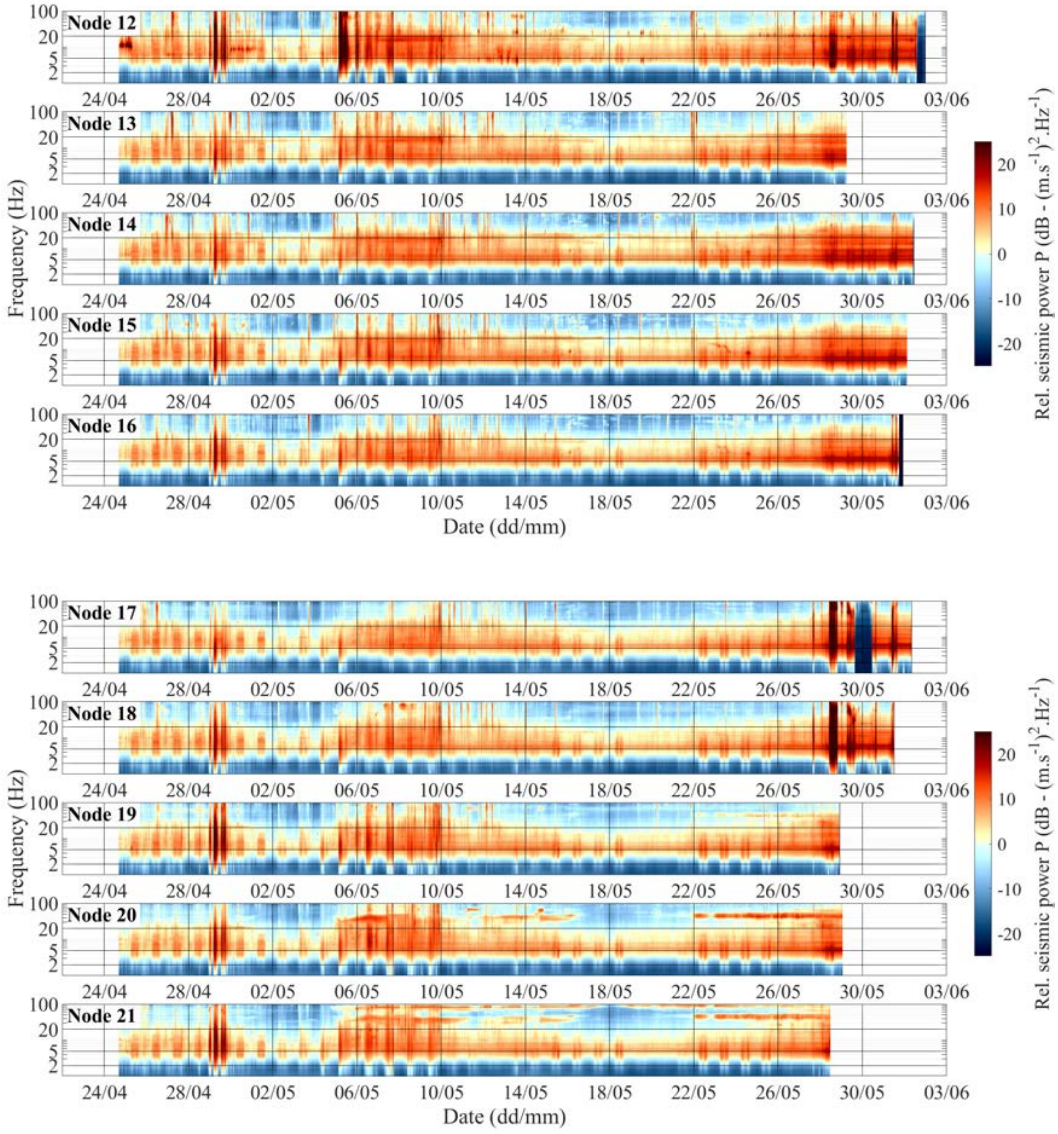
Node 12
Node 13
Node 14
Node 15
Node 16
Node 17
Node 18
Node 19
Node 20
Node 21
Frequency (Hz)
100
20
5
2
24/04
28/04
02/05
06/05
10/05
14/05
18/05
22/05
26/05
30/05
03/06
Date (dd/mm)
Rel. seismic power P (dB - (m.s-1)2.Hz-1)
20
10
0
-10
-20

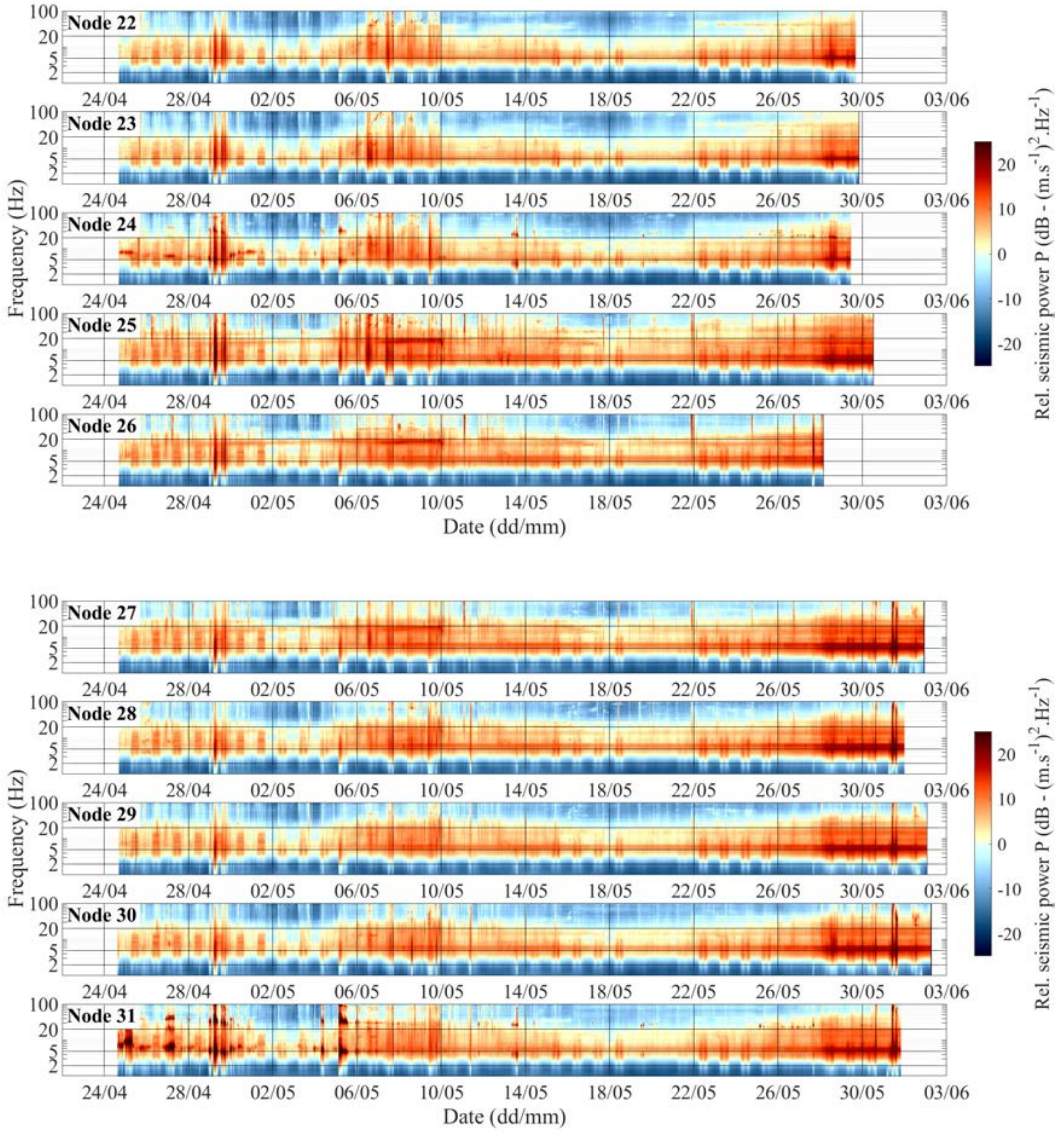
Node 22
Node 23
Node 24
Node 25
Node 26
Node 27
Node 28
Node 29
Node 30
Node 31
100
20
5
2
Frequency (Hz)
24/04
28/04
02/05
06/05
10/05
14/05
18/05
22/05
26/05
30/05
03/06
Date (dd/mm)
20
10
0
-10
-20
Rel. seismic power P (dB - (m.s-1)2.Hz-1)

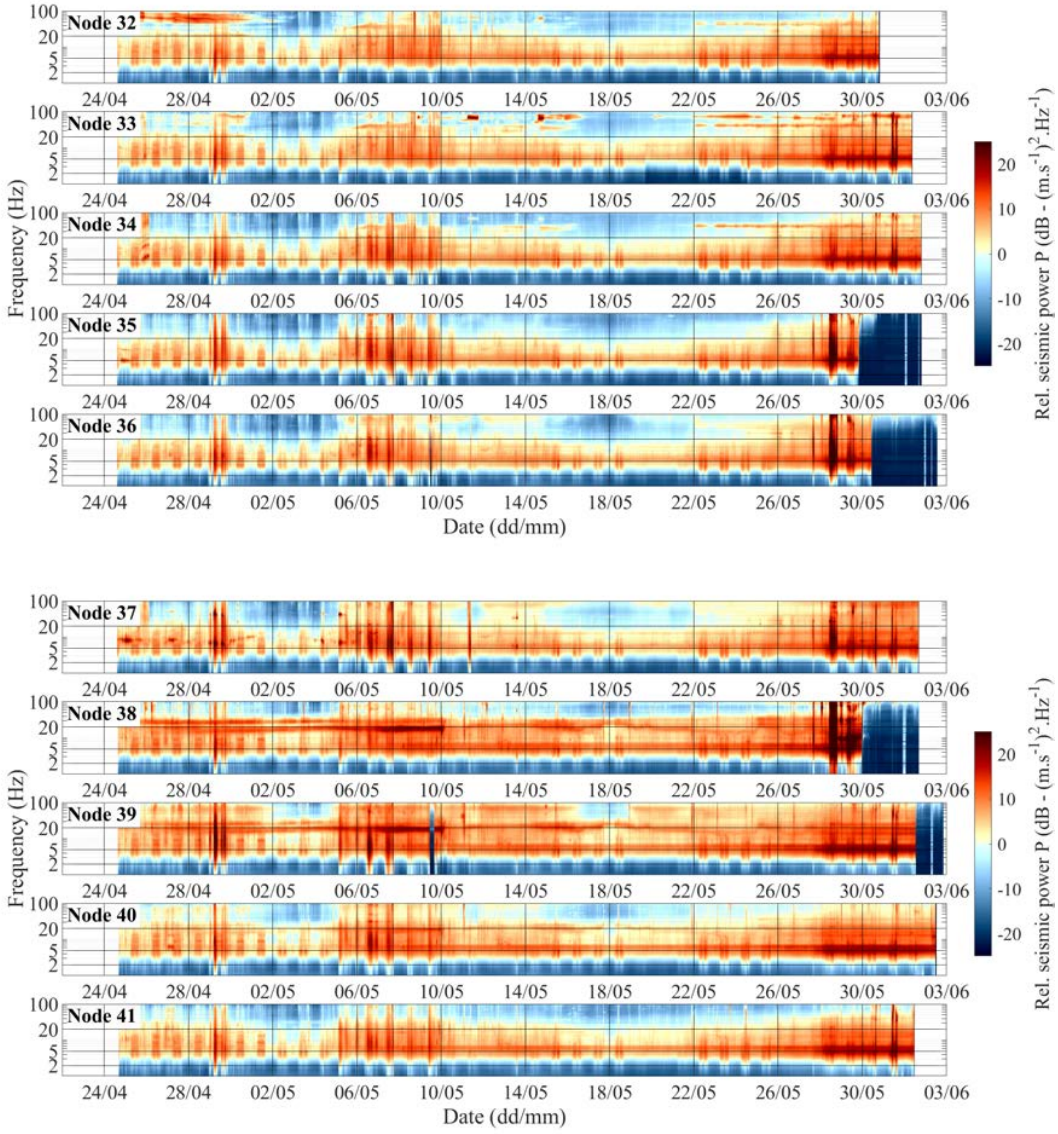
Node 32
Node 33
Node 34
Node 35
Node 36
Node 37
Node 38
Node 39
Node 40
Node 41
100
20
5
2
Frequency (Hz)
24/04
28/04
02/05
06/05
10/05
14/05
18/05
22/05
26/05
30/05
03/06
Date (dd/mm)
20
10
0
-10
-20
Rel. seismic power P (dB - (m.s-1)2.Hz-1)

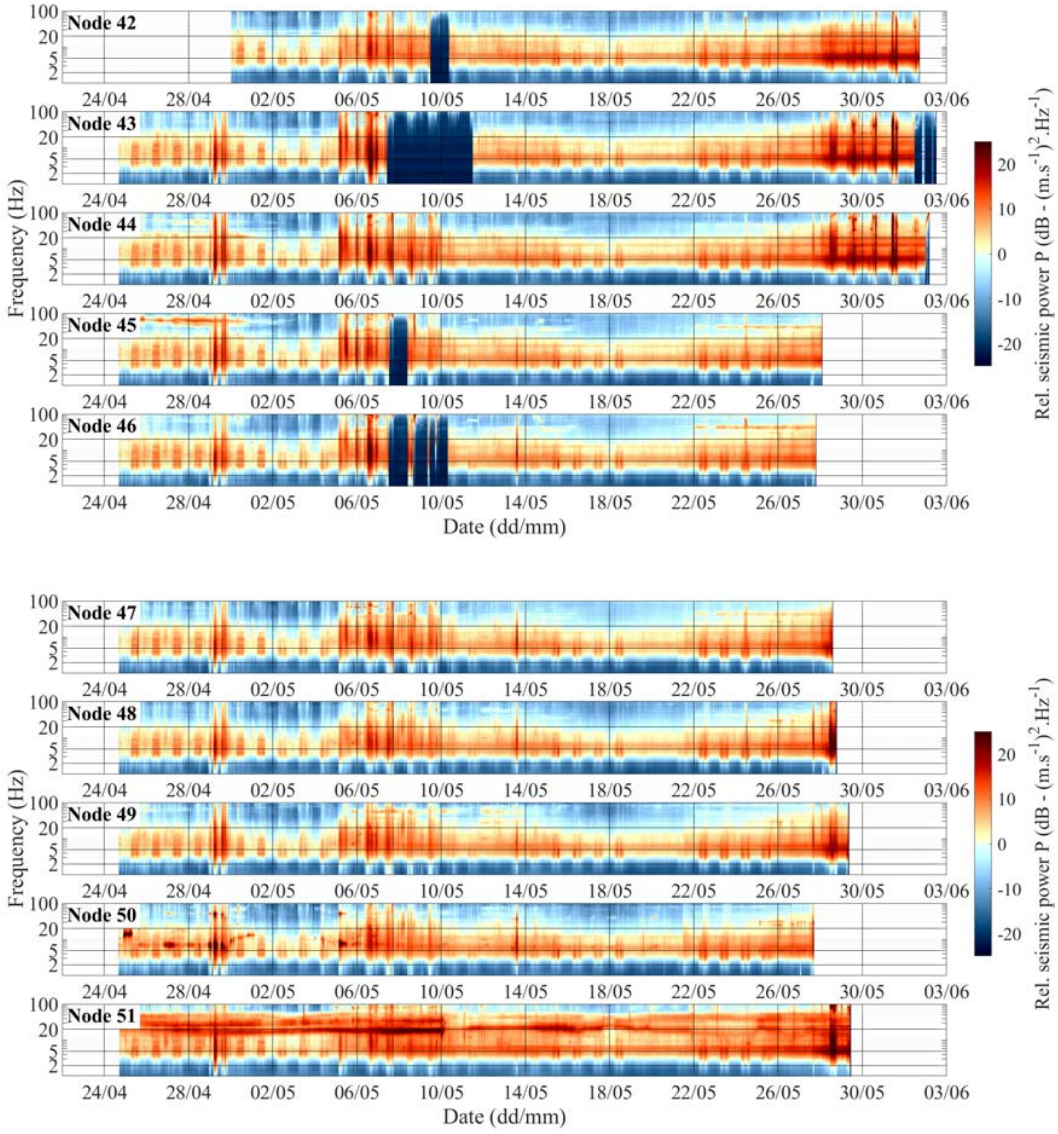
Node 42
Node 43
Node 44
Node 45
Node 46
Node 47
Node 48
Node 49
Node 50
Node 51
100
20
5
2
24/04
28/04
02/05
06/05
10/05
14/05
18/05
22/05
26/05
30/05
03/06
Frequency (Hz)
Date (dd/mm)
20
10
0
-10
-20
Rel. seismic power P (dB - (m.s-1)2.Hz-1)

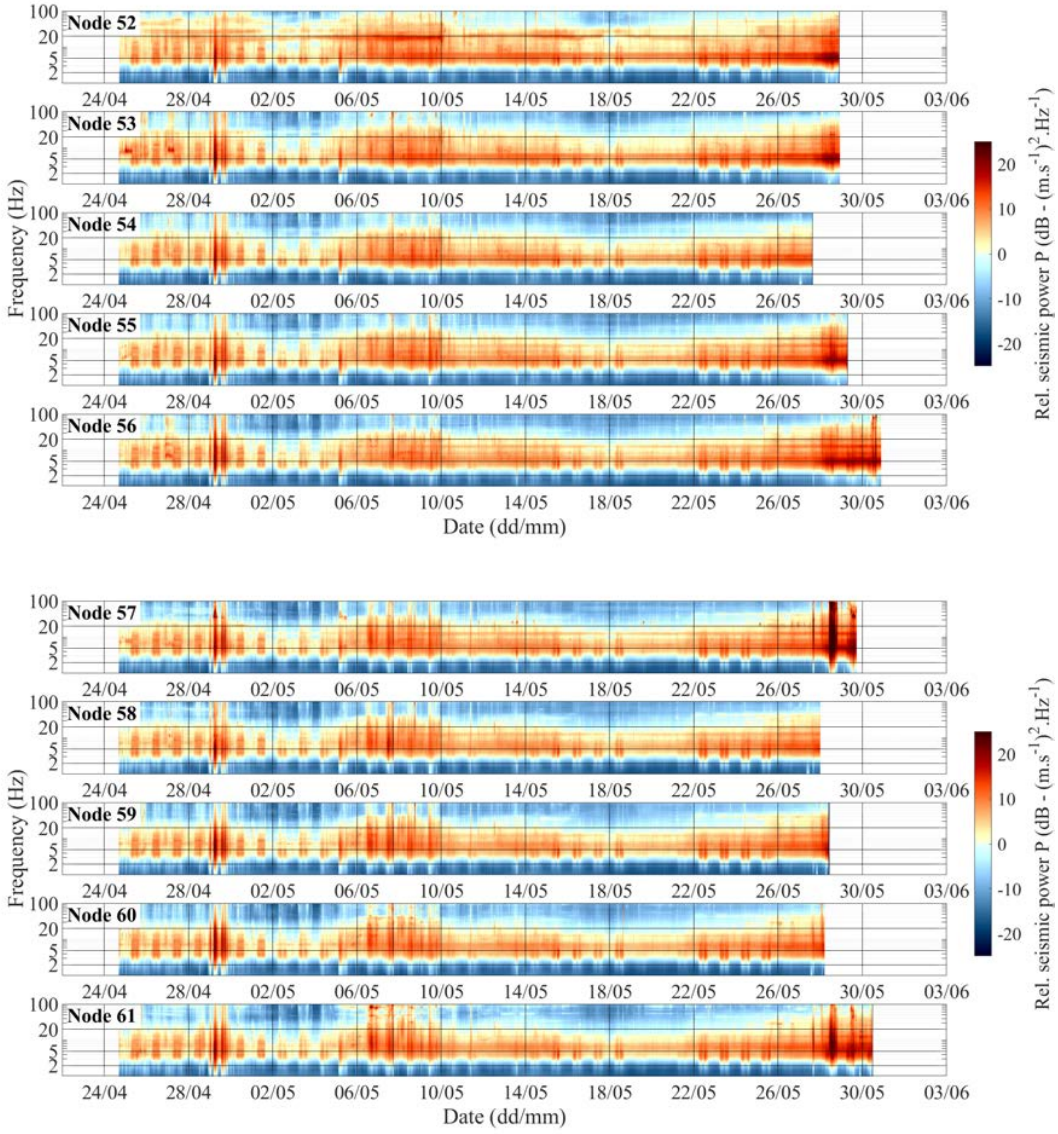
Node 52
Node 53
Node 54
Node 55
Node 56
Node 57
Node 58
Node 59
Node 60
Node 61
100
20
5
2
24/04
28/04
02/05
06/05
10/05
14/05
18/05
22/05
26/05
30/05
03/06
Frequency (Hz)
Date (dd/mm)
20
10
0
-10
-20
Rel. seismic power P (dB - (m.s-1)2.Hz-1)

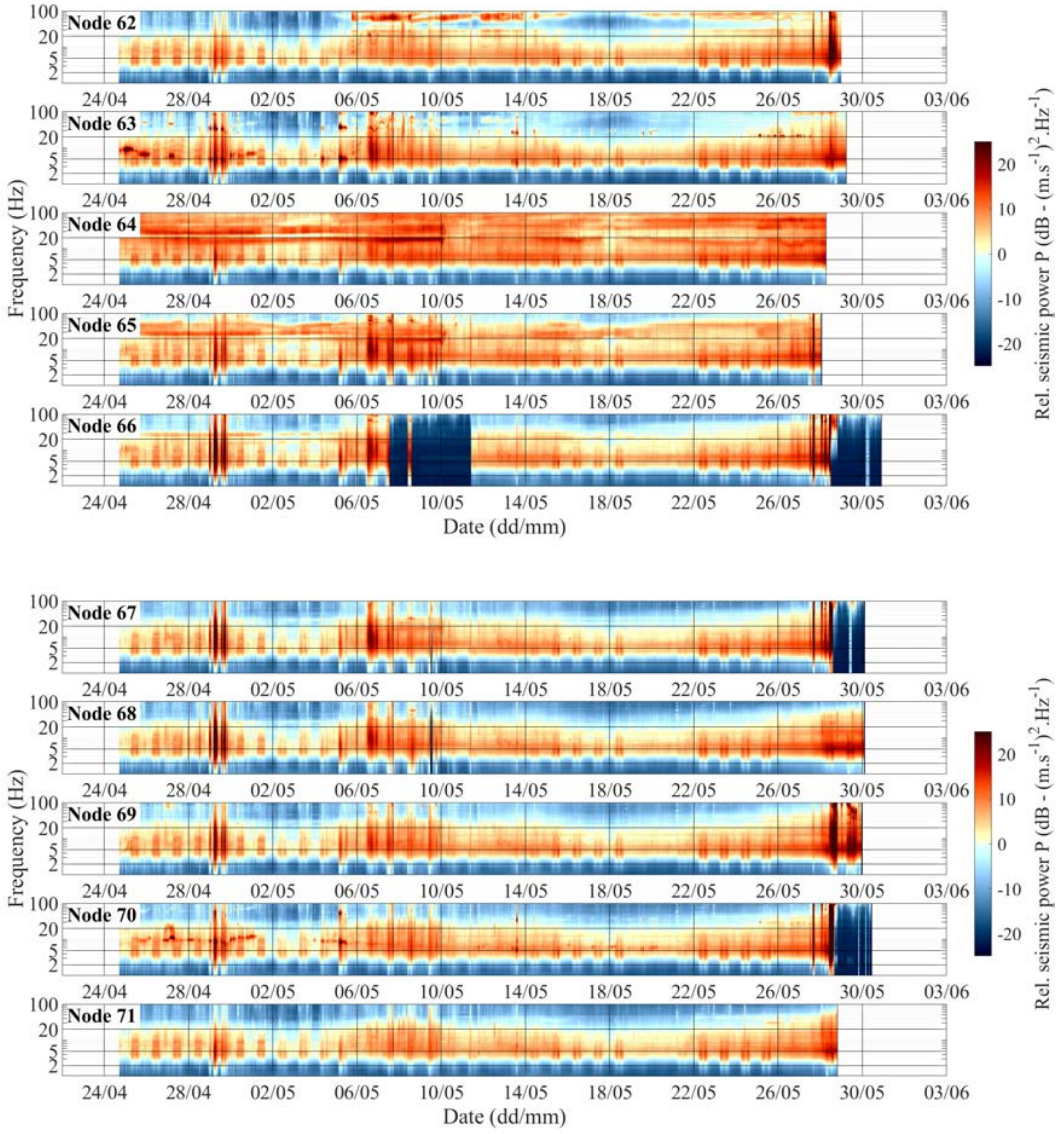
Node 62
Node 63
Node 64
Node 65
Node 66
Node 67
Node 68
Node 69
Node 70
Node 71
100
20
5
2
Frequency (Hz)
24/04
28/04
02/05
06/05
10/05
14/05
18/05
22/05
26/05
30/05
03/06
Date (dd/mm)
20
10
0
-10
-20
Rel. seismic power P (dB - (m.s-1)2.Hz-1)

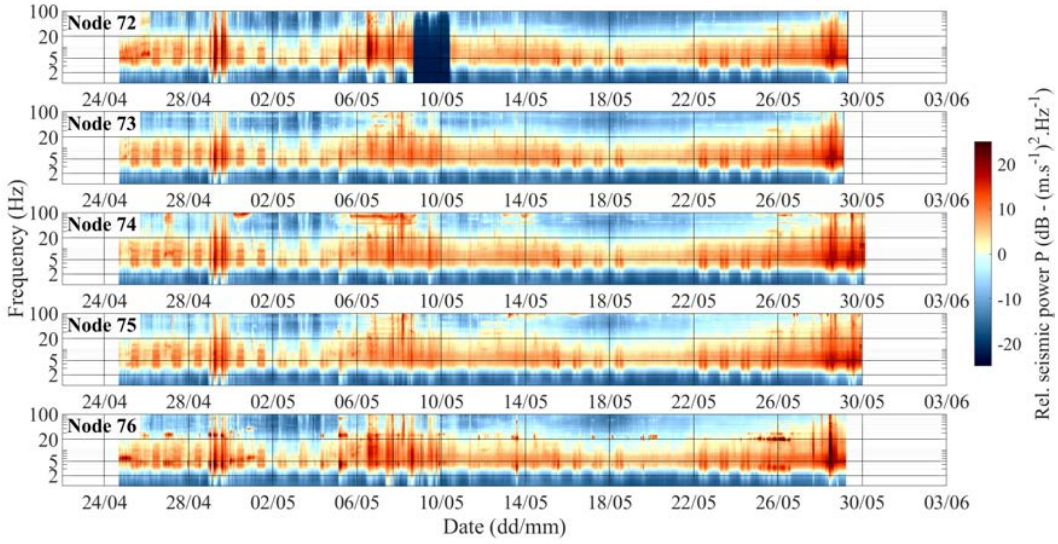
Node 72
Node 73
Node 74
Node 75
Node 76
Frequency (Hz)
100
20
5
2
24/04
28/04
02/05
06/05
10/05
14/05
18/05
22/05
26/05
30/05
03/06
Date (dd/mm)
Rel. seismic power P (dB - (m.s-1)2.Hz-1)
20
10
0
-10
-20

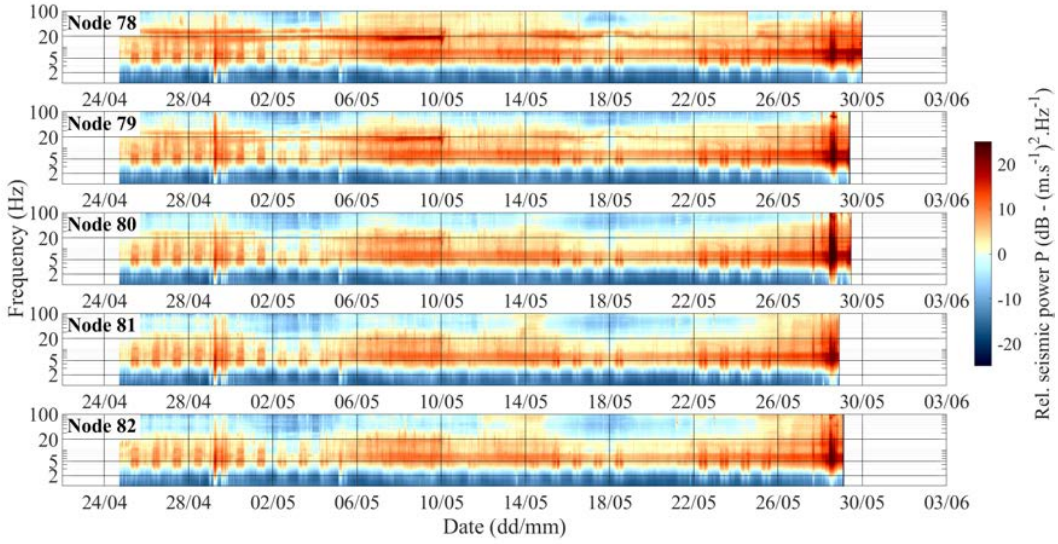
Node 78
Node 79
Node 80
Node 81
Node 82
Frequency (Hz)
100
20
5
2
24/04
28/04
02/05
06/05
10/05
14/05
18/05
22/05
26/05
30/05
03/06
Date (dd/mm)
Rel. seismic power P (dB - (m.s-1)2.Hz-1)
20
10
0
-10
-20

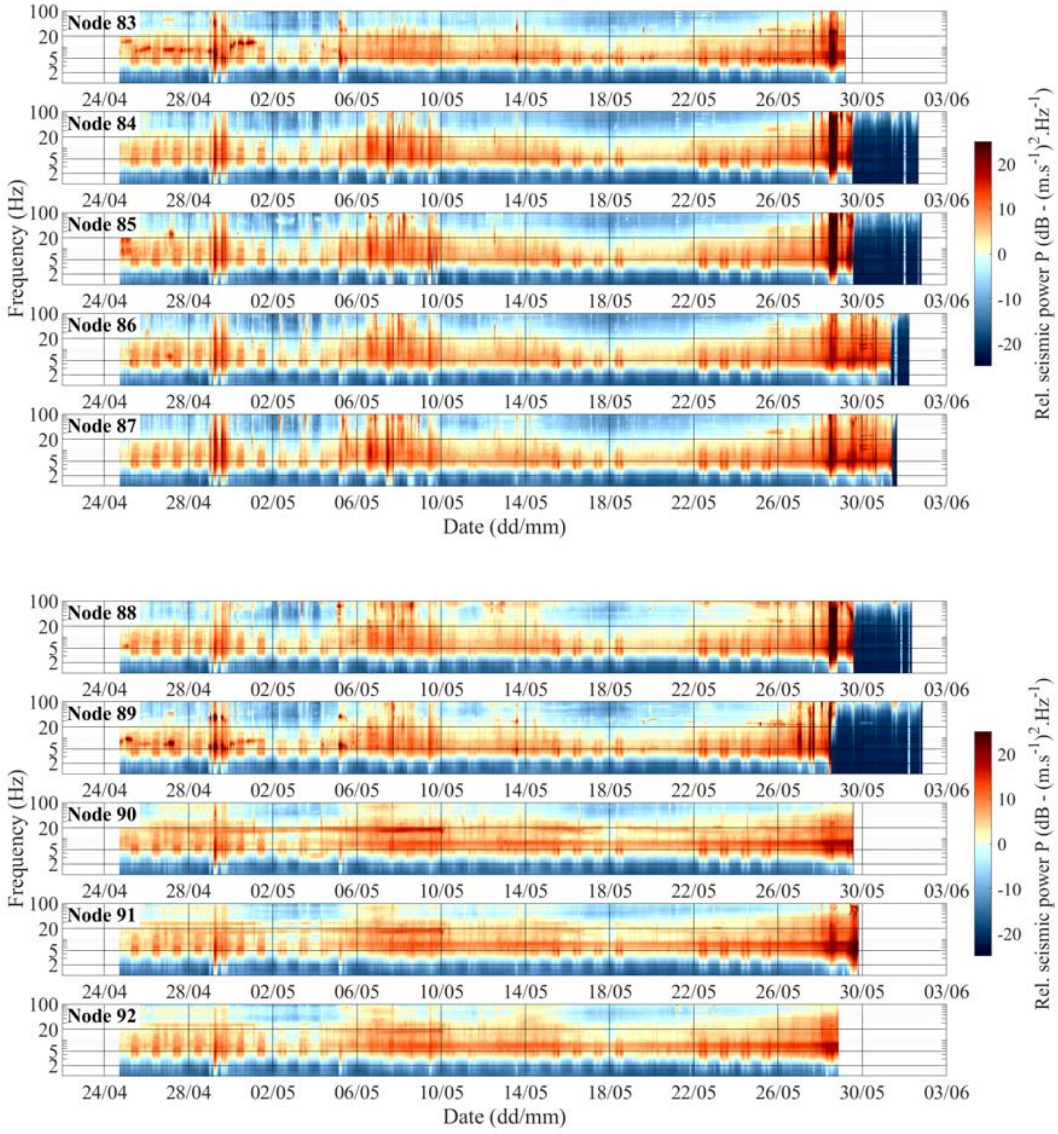
Node 83
Node 84
Node 85
Node 86
Node 87
Node 88
Node 89
Node 90
Node 91
Node 92
100
20
5
2
24/04
28/04
02/05
06/05
10/05
14/05
18/05
22/05
26/05
30/05
03/06
Frequency (Hz)
Date (dd/mm)
20
10
0
-10
-20
Rel. seismic power P (dB - (m.s-1)2.Hz-1)

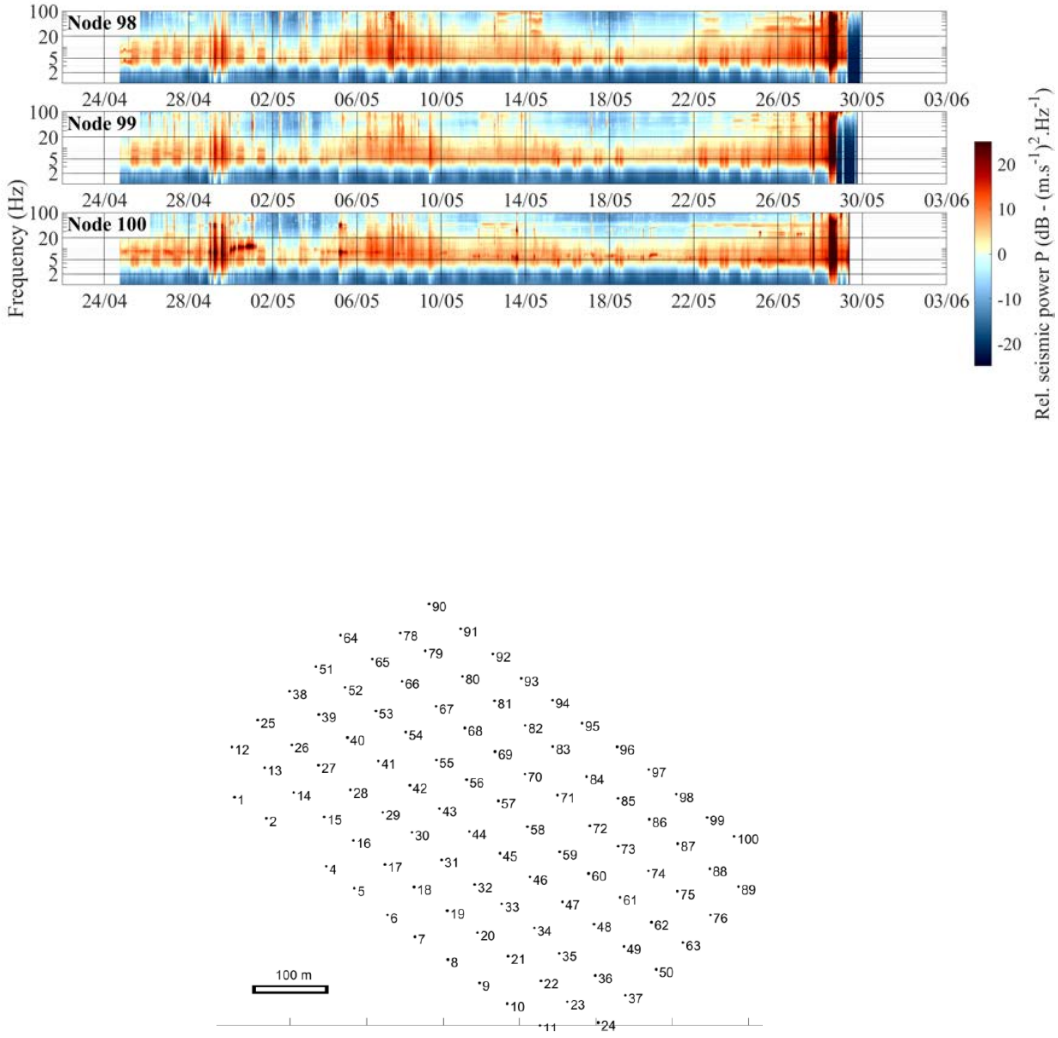


Fig. S1: Spectrograms calculated at all stations over the whole period. The lower panel shows a map view of the node number nomenclature. The reader should refer to Fig. 1 for absolute positioning of the dense array. The color scale represents seismic power, as calculated in Fig. 4, and is identic across all panels.